

# **Determination of the beam asymmetry $\Sigma$ in $\eta$ - and $\eta'$ -photoproduction using Bayesian statistics**

JAKOB MICHAEL KRAUSE

Masterarbeit in Physik

angefertigt im Helmholtz-Institut für Strahlen- und  
Kernphysik

vorgelegt der

Mathematisch-Naturwissenschaftlichen Fakultät  
der  
Rheinischen Friedrich-Wilhelms-Universität  
Bonn

Sep 2022

DRAFT

I hereby declare that this thesis was formulated by myself and that no sources or tools other than those cited were used.

Bonn, .....  
Date .....  
Signature

1. Gutachterin: JUN. PROF. DR. ANNIKA THIEL
2. Gutachter: PROF. DR. JOCHEN DINGFELDER

DRAFT

# Contents

---

<b>1</b>	<b>Introduction</b>	<b>1</b>
1.1	Photoproduction of Pseudoscalar Mesons . . . . .	4
1.2	Measurement of Polarization Observables . . . . .	5
1.3	Introduction to BAYESIAN statistics . . . . .	5
1.3.1	Frequentist Approach . . . . .	5
1.3.2	Bayesian approach . . . . .	5
1.3.3	Combining inferences . . . . .	5
1.4	Motivation and Structure of this Thesis . . . . .	5
<b>2</b>	<b>Experimental Setup</b>	<b>7</b>
2.1	Production of (polarized) high energy photon beam . . . . .	7
2.1.1	Tagger . . . . .	8
2.2	Beam Target . . . . .	8
2.3	Calorimeters . . . . .	8
2.4	Trigger . . . . .	8
<b>3</b>	<b>Event selection</b>	<b>11</b>
3.1	Reconstruction of events . . . . .	12
3.2	Preselection and charge cut . . . . .	12
3.3	Time of particles . . . . .	13
3.4	Kinematic constraints . . . . .	15
3.4.1	Derivation of cut conditions . . . . .	15
3.4.2	Determination of cut ranges . . . . .	16
3.4.3	Quality of event selection . . . . .	21
3.5	Investigation of background and additional cuts . . . . .	23
3.5.1	Inspecting plausibility of background reactions . . . . .	23
3.5.2	Misidentification of background reactions . . . . .	26
3.5.3	Examination of additional cuts . . . . .	31
3.6	Summary of event selection . . . . .	34
3.6.1	Reaction $\gamma p \rightarrow p\eta' \rightarrow p\gamma\gamma$ . . . . .	34
3.6.2	Reaction $\gamma p \rightarrow p\eta \rightarrow p\gamma\gamma$ . . . . .	35
<b>4</b>	<b>Extraction of the beam asymmetries <math>\Sigma_\eta</math> and <math>\Sigma_{\eta'}</math></b>	<b>37</b>
4.1	Methods . . . . .	38
4.1.1	Event yield asymmetries . . . . .	38
4.1.2	Event based fit . . . . .	41

4.2	Determination of $\Sigma_\eta$ using Bayesian statistics . . . . .	44
4.2.1	Application of methods to toy Monte Carlo data . . . . .	44
4.2.2	Application of methods to data . . . . .	53
4.2.3	Discussion . . . . .	56
4.3	Determination of $\Sigma_{\eta'}$ . . . . .	58
4.3.1	Application of event based fit to toy Monte Carlo data . . . . .	58
4.3.2	Application of event based fit to data . . . . .	64
4.3.3	Systematic error . . . . .	68
<b>5</b>	<b>Summary and outlook</b>	<b>63</b>
<b>A</b>	<b>Additional plots and calculations</b>	<b>65</b>
A.1	Statistical error for the asymmetry $A(\phi)$ . . . . .	65
A.2	Kinematic variables for each bin . . . . .	67
A.2.1	Coplanarity . . . . .	67
A.2.2	Polar angle difference . . . . .	69
A.2.3	Missing mass . . . . .	71
A.2.4	Invariant mass . . . . .	73
<b>B</b>	<b>Discussion of binned fits</b>	<b>75</b>
<b>C</b>	<b>Investigation of posteriors without truncation</b>	<b>77</b>
<b>Bibliography</b>		<b>81</b>
<b>List of Figures</b>		<b>83</b>
<b>List of Tables</b>		<b>89</b>

# CHAPTER 4

## Extraction of the beam asymmetries $\Sigma_\eta$ and $\Sigma_{\eta'}$

The beam asymmetry  $\Sigma$  is observable when a linearly polarized photon beam and unpolarized liquid hydrogen target are employed [san]. The polarized differential cross section  $\frac{d\sigma}{d\Omega_{\text{pol}}}$  is not symmetric in the azimuthal angle  $\phi$  anymore as opposed to the unpolarized differential cross section  $\frac{d\sigma}{d\Omega_0}$ . It is rather modulated by a cosine dependence which scales with the polarization observable  $\Sigma$  and the (linear) beam polarization  $p_\gamma$ , see equation (4.1) [san].

$$\frac{d\sigma}{d\Omega_{\text{pol}}} (E_\gamma, \cos \theta, \phi) = \frac{d\sigma}{d\Omega_0} (E_\gamma, \cos \theta) \cdot \left[ 1 - p_\gamma \Sigma (E_\gamma, \cos \theta) \cos(2\varphi) \right] \quad (4.1)$$

Since the incident photon beam is polarized, photon momentum  $\vec{k}$  and polarization  $\vec{\epsilon}$  span a plane which is referred to as the beam polarization plane. This plane is tilted by the angle  $\varphi$  with respect to the reaction plane which is defined by the final state momenta. Naturally, this plane builds the angle  $\phi$  in the laboratory system. At the same time the angle of the beam polarization plane in the same reference frame is defined as  $\alpha$ . It holds

$$\varphi = \alpha - \phi. \quad (4.2)$$

Figure 4.1 illustrates definitions of all angles and planes. Theoretically the beam asymmetry can be

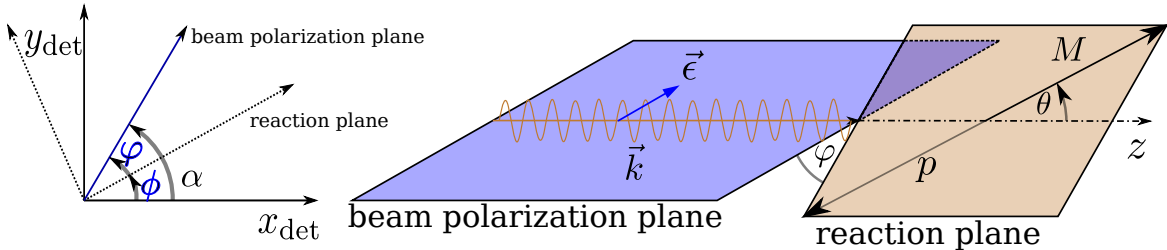


**Figure 4.1:** Left: Definition of angles  $\alpha, \phi, \varphi$ . Right: Photon momentum  $\vec{k}$  and polarization  $\vec{\epsilon}$  define the beam polarization plane while the reaction plane is defined by the recoil proton  $p$  and produced meson  $M$ .

determined by a measurement of the cross section and a fit using equation (4.1). However, when calculating polarized cross sections, it is important to have good control over flux normalization and detector acceptance in three dimensions  $(E_\gamma, \cos \theta, \phi)$  to minimize systematical errors. To avoid

this, the measurement of asymmetries can be used to access the polarization observable  $\Sigma$  instead. Particularly, data is taken for two distinct orthogonal polarization settings corresponding to  $\alpha = \pm 45^\circ$ .

This chapter will illustrate the process of determining the beam asymmetry for  $\eta$  and  $\eta'$  photoproduction. The published results of  $\Sigma_\eta$  [eta; Afz19] are used to check the accuracy and functionality of employed bayesian methods. Bayesian methods, as well as traditional frequentist approaches are used afterwards to extract new results for  $\Sigma_{\eta'}$ . First, the determination of the beam photon polarization is briefly described, then the used methods will be presented and subsequently their application for each final state, respectively.

## 4.1 Methods

The beam asymmetry has to be determined via fits to  $\phi$  distributions obtained from data. These are performed as either binned or unbinned fits. Both methods allow the application of Bayesian methods as will be discussed in the following. Additionally the advantages and disadvantages off all methods are compared.

### 4.1.1 Event yield asymmetries

Measurements were made in two distinct polarization settings  $\alpha = \pm 45^\circ = \alpha^{\perp/\parallel}$ . Thus, the polarized cross sections for both settings are given by<sup>1</sup>

$$\frac{d\sigma}{d\Omega_{\text{pol}}}^{\parallel} = \frac{d\sigma}{d\Omega_0} \cdot \left[ 1 - p_\gamma^{\parallel} \Sigma \cos(2(\alpha^{\parallel} - \phi)) \right] \quad (4.3)$$

and

$$\frac{d\sigma}{d\Omega_{\text{pol}}}^{\perp} = \frac{d\sigma}{d\Omega_0} \cdot \left[ 1 - p_\gamma^{\perp} \Sigma \cos(2(\alpha^{\perp} - \phi)) \right] \quad (4.4)$$

$$= \frac{d\sigma}{d\Omega_0} \cdot \left[ 1 + p_\gamma^{\perp} \Sigma \cos(2(\alpha^{\parallel} - \phi)) \right]. \quad (4.5)$$

Note that equation (4.5) holds, because

$$\alpha^{\perp} = \alpha^{\parallel} + \pi/2 \quad \text{and} \quad \cos x = -1 \cdot \cos(x + \pi).$$

Consider now taking the difference of equations (4.3) and (4.5)

$$\frac{d\sigma}{d\Omega_{\text{pol}}}^{\perp} - \frac{d\sigma}{d\Omega_{\text{pol}}}^{\parallel} = \frac{d\sigma}{d\Omega_0} \cdot \left( p_\gamma^{\perp} + p_\gamma^{\parallel} \right) \Sigma \cos(2(\alpha^{\parallel} - \phi)). \quad (4.6)$$

One can further eliminate the unpolarized cross section from this equation by dividing by the polarization weighted sum of equations (4.3) and (4.5)

$$\alpha \cdot \frac{d\sigma}{d\Omega_{\text{pol}}}^{\perp} + \beta \cdot \frac{d\sigma}{d\Omega_{\text{pol}}}^{\parallel} = \frac{d\sigma}{d\Omega_0} \cdot \left[ \alpha + \beta - \left( \alpha p_\gamma^{\perp} - \beta p_\gamma^{\parallel} \right) \Sigma \cos(2(\alpha^{\parallel} - \phi)) \right] \stackrel{!}{=} 2 \frac{d\sigma}{d\Omega_0}. \quad (4.7)$$

<sup>1</sup> The dependencies of polarized and unpolarized cross sections as well as the beam asymmetry like in equation (4.1) are implied.

Since

$$\frac{d}{d\phi} \frac{d\sigma}{d\Omega_0} \stackrel{!}{=} 0 \forall \phi,$$

it holds

$$\alpha p_\gamma^{\parallel} - \beta p_\gamma^{\perp} \stackrel{!}{=} 0 \quad \alpha + \beta \stackrel{!}{=} 2, \quad (4.8)$$

such that

$$\alpha = \frac{2p_\gamma^{\parallel}}{p_\gamma^{\perp} + p_\gamma^{\parallel}} \quad \beta = \frac{2p_\gamma^{\perp}}{p_\gamma^{\perp} + p_\gamma^{\parallel}}. \quad (4.9)$$

The beam asymmetry  $\Sigma$  is thus accessible via the asymmetry

$$A(\phi) = \frac{\frac{d\sigma^{\perp}}{d\Omega \text{ pol}} - \frac{d\sigma^{\parallel}}{d\Omega \text{ pol}}}{p_\gamma^{\parallel} \frac{d\sigma^{\perp}}{d\Omega \text{ pol}} + p_\gamma^{\perp} \frac{d\sigma^{\parallel}}{d\Omega \text{ pol}}} = \Sigma \cos(2(\alpha^{\parallel} - \phi)). \quad (4.10)$$

At this point one can now make use of the fact that in any scattering reaction the number of events  $N$  is given by the product of luminosity  $L$  and total cross section  $\sigma$  [povh]

$$N = L \cdot \sigma = \Phi \cdot N_t \cdot \frac{d\sigma}{d\Omega} \cdot \Delta\Omega,$$

where  $\Phi$  is the beam flux,  $N_t$  the number of target particles and  $\Delta\Omega$  is the solid angle covered by the detector. Substituting this in equation (4.10) one can build the asymmetry  $A(\phi)$  using only the (flux-)normalized event yields  $\tilde{N}^{\parallel/\perp}(E_\gamma, \cos\theta, \phi)^2$

$$A(\phi) = \frac{\tilde{N}^{\perp} - \tilde{N}^{\parallel}}{p_\gamma^{\parallel} \tilde{N}^{\perp} + p_\gamma^{\perp} \tilde{N}^{\parallel}} = \Sigma \cos(2(\alpha^{\parallel} - \phi)). \quad (4.11)$$

Alternatively, the event yields  $N$  can also be normalized by integrating over the total azimuthal angle range in each bin of  $(E_\gamma, \cos\theta)$ . This normalization technique has been used in reference [Afz19] and will also be used in this work. Using appropriate binning in  $\phi$  in addition to beam energy and meson polar angle the asymmetry can be build for all kinematic bins and the beam asymmetry then be extracted via a one-Parameter fit. The statistical errors for  $A(\phi)$  are given by GAUSSIAN error propagation (see appendix A.1).

## Frequentist

The beam asymmetry can now be determined via a frequentist fit, where  $\Sigma$  is determined such that the  $\chi^2$  value resulting from the data points and equation 4.11 is minimized. The results are point estimates with statistical error bars that are also obtained from the fit:  $\hat{\Sigma} \pm \sigma_{\hat{\Sigma}}$ . One can show that the probability distribution of the  $\chi^2$  value, given  $n$  degrees of freedom, has mean  $n$  and variance  $2n$  [statistics]. This

---

<sup>2</sup> Again, arguments  $(E_\gamma, \cos\theta, \phi)$  are implied.

means  $\chi^2/\text{NDF} \approx 1$  may be verified in order to diagnose the fit itself. Much larger values indicate a bad fit and much smaller values an overestimation of errors [statistics]. Multiple automated minimization and calculation algorithms for  $\chi^2$  fitting are available as open source. The *Python* [python] module *scipy* [scipy] and *ROOT* [root] offer e.g. the methods `scipy.optimize.curve_fit` [**pFit**] and `TH1::Fit() [rFit]` for discrete/binned data, which were used in the analysis.

## BAYESIAN

Following section 1.3, where the basics of BAYESIAN inference were discussed, the goal of a BAYESIAN approach is to sample marginal posterior distributions for each fitted parameter from the joint posterior  $p(\theta|y)$  which depends on the observed data  $y$ . The joint posterior itself is proportional to the product of priors  $\pi(\theta)$  and likelihood  $\mathcal{L}(y|\theta)$  (BAYES' theorem). This collapses to a one parameter problem in the case of fitting the event yield asymmetries (Eq. (4.11))

$$p(\Sigma|y) \propto \pi(\Sigma) \cdot \mathcal{L}(y|\Sigma). \quad (4.12)$$

However, to be able to sample from a joint posterior, prior and likelihood need to be specified. In order not to bias the fit towards any particular values, the prior is chosen weakly-informative [bayes], realized by a broad GAUSSIAN centered at 0 which is truncated to the physically allowed parameter space of  $\Sigma \in [-1, 1]$ . An improper uniform prior is avoided this way following the recommendations of reference [standevs] although the model would in principle be suited since the beam asymmetry is designed to be constrained to a finite interval [standevs]. Furthermore, the likelihood is formulated assuming GAUSSIAN errors  $\epsilon_n$  at each data point  $y_n$ , which should be described by the asymmetry (Eq (4.11)) at bin  $n$   $A(\phi_n; \Sigma)$ , i. e.<sup>3</sup>

$$\Sigma \sim \mathcal{N}(0, 1)_{[-1, 1]} \quad y_n = A(\phi_n; \Sigma) + \epsilon_n \quad \epsilon_n \sim \mathcal{N}(0, \sigma_n), \quad (4.13)$$

which is equivalent to

$$\Sigma \sim \mathcal{N}(0, 1) \quad y_n \sim \mathcal{N}(A(\phi_n; \Sigma), \sigma_n). \quad (4.14)$$

Assuming all data points are independent, the likelihood of all data points now evaluates to the product of the likelihood at each data point  $y_n$  and the posterior results in

$$p(\Sigma|y) \propto \pi(\Sigma) \cdot \mathcal{L}(y|\Sigma) = \mathcal{N}(\Sigma|0, 1)_{[-1, 1]} \cdot \prod_n \mathcal{N}(y_n|A(\phi_n; \Sigma), \sigma_n) \quad (4.15)$$

$$\Leftrightarrow -\ln p(\Sigma|y) = \frac{1}{2}\Sigma^2 + \frac{1}{2} \sum_n \left( \frac{y_n - A(\phi_n; \Sigma)}{\sigma_n} \right)^2 + \text{constant terms}, \quad (4.16)$$

such that all ingredients are present to form a fully BAYESIAN probabilistic model<sup>4</sup>. This model was implemented in Stan [stan], directly giving access to samples from the posterior obtained with the No-U-Turn-Sampler (NUTS) [stan; nuts]. Hereby, the sampling is restricted to the allowed parameter

<sup>3</sup> Remember the notation introduced in section 1.3:  $x \sim \mathcal{N}(\mu, \sigma) = \mathcal{N}(x|\mu, \sigma) = \frac{1}{\sqrt{2\pi}\sigma} e^{-\frac{(x-\mu)^2}{2\sigma^2}}$ .

<sup>4</sup> Note that the sampling aims only to reflect the right proportionality of the (marginal) posterior. Thus, constant terms can be dropped and are of no further interest [stan].

region  $\Sigma \in [-1, 1]$ . As a measure of goodness of fit, the  $p$ -values obtained from the posterior predictive distributions, as introduced in section 1.3, are reviewed. To diagnose the convergence of the MCMC fit, sensible values for  $\hat{R}$  and the Monte-Carlo standard error  $\sigma_{\text{MCSE}}$  are verified.

### 4.1.2 Event based fit

Although intuitive and easily implementable the binned fit –BAYESIAN or not– has one critical disadvantage: it is inevitable that information is lost because the asymmetry  $A(\phi)$  is a binned quantity and hence, the choice of binning influences the fit results. This is discussed in more detail in appendix B. Especially kinematic bins with low statistics show this behavior. To circumvent this problem, an *unbinned fit*, based on the likelihood function for each event, can be performed. Also, no assumptions on the distribution of statistical errors have to be made since each event is taken into account individually. Yet, the event based fit does not provide any measure of goodness of fit, so that the study of toy Monte Carlo data is essential when checking the working principle of the method.

In a polarized experiment the azimuthal angle distribution of events is not isotropic, but modulated by a cosine term coupling to beam asymmetry  $\Sigma$  and beam polarization  $p_\gamma^{\parallel/\perp}$  for each setting  $\alpha^{\parallel/\perp}$ , as is expressed through the respective differential cross sections in Equations 4.3 and 4.4. Since the number of events is proportional to the cross section, the probability  $p(\phi, p_\gamma^{\parallel/\perp} | \Sigma)$  to find an event under the azimuthal angle  $\phi$  for a given bin of  $(E_\gamma, \cos \theta)$  and setting  $\alpha^{\parallel/\perp}$  is<sup>5</sup>

$$p(\phi, p_\gamma^{\parallel/\perp} | \Sigma) = \frac{\left[ 1 \mp p_\gamma^{\parallel/\perp} \Sigma \cos(2(\alpha^\parallel - \phi)) \right]}{\frac{1}{2\pi} \int_0^{2\pi} d\phi \left[ 1 \mp p_\gamma^{\parallel/\perp} \Sigma \cos(2(\alpha^\parallel - \phi)) \right]}. \quad (4.17)$$

This is only true for an idealized experiment with acceptance  $\epsilon = \text{const} \forall \phi$ , so that the acceptance  $\epsilon(\phi)$  has to be included in the probability for each event. As demonstrated in reference [Har17] a FOURIER series truncated after the fourth order is sufficient to model any occurring function

$$\epsilon(\phi) = \sum_{k=0}^4 a_k \sin(k\phi) + b_k \cos(k\phi),$$

where the eight detector coefficients  $a_k$  and  $b_k$  are determined from the fit. With this the measurable probability  $\tilde{p}(\phi, p_\gamma^{\parallel/\perp} | \Sigma, a, b)$  is

$$\tilde{p}(\phi, p_\gamma^{\parallel/\perp} | \Sigma, a, b) \propto \left[ 1 \mp p_\gamma^{\parallel/\perp} \Sigma \cos(2(\alpha^\parallel - \phi)) \right] \cdot \epsilon(\phi) \quad (4.18)$$

$$= \left[ 1 \mp p_\gamma^{\parallel/\perp} \Sigma \cos(2(\alpha^\parallel - \phi)) \right] \cdot \left( \sum_{k=0}^4 a_k \sin(k\phi) + b_k \cos(k\phi) \right), \quad (4.19)$$

---

<sup>5</sup> Note: Normalizing  $p(\phi, p_\gamma^{\parallel/\perp} | \Sigma)$  to  $2\pi$  (or any other arbitrary constant) is sufficient for the fit as long as the integral does not depend on the fit parameters. The normalization to  $2\pi$  is chosen for better readability. However, to calculate actual probabilities, one must multiply Eq. (4.17) by  $2\pi$ .

where  $a := \{a_k\}_{k=0}^4$ ,  $b := \{b_k\}_{k=0}^4$ . Finally, normalizing  $\frac{1}{2\pi} \int_0^{2\pi} d\phi \tilde{p}(\phi, p_\gamma^{\parallel/\perp} | \Sigma, a, b) = 1$ ,

$$\tilde{p}(\phi, p_\gamma^{\parallel/\perp} | \Sigma, a, b) = \frac{\left[1 \mp p_\gamma^{\parallel/\perp} \Sigma \cos(2(\alpha^\parallel - \phi))\right] \cdot \left(\sum_{k=0}^4 a_k \sin(k\phi) + b_k \cos(k\phi)\right)}{1 \pm \frac{1}{2} a_2 p_\gamma^{\parallel/\perp} \Sigma}. \quad (4.20)$$

The respective polarization setting  $\alpha^{\parallel/\perp}$  determines the sign in the normalizing constant which allows an uncorrelated estimation of the detector coefficient  $a_2$  and the beam asymmetry  $\Sigma$ . To simplify notation and implementation, Equation (4.21) can be written as *one* probability for all events – regardless of polarization setting – if the polarization values  $p_\gamma^{\parallel}$  are multiplied by  $(-1)$  and summarized as  $p_\gamma$ :

$$\tilde{p}(\phi, p_\gamma | \Sigma, a, b) = \frac{\left[1 + p_\gamma \Sigma \cos(2(\alpha - \phi))\right] \cdot \left(\sum_{k=0}^4 a_k \sin(k\phi) + b_k \cos(k\phi)\right)}{1 - \frac{1}{2} a_2 p_\gamma \Sigma}, \quad (4.21)$$

with  $\alpha = -45^\circ$  fixed.

In section 3.3 the subtraction of uncorrelated time background was discussed via a sideband subtraction. Naturally, without binning the data, this strategy is invalid and prompt peak and sideband events have to be fitted simultaneously. Hereby it is important to consider that the random time background is realized as flat distribution underneath the complete reaction time spectrum (cf. Figure 3.3), *including* the range of the prompt peak. The fraction of true coincident events to random coincidences is given as

$$f = \frac{N_{\text{prompt}} - w \cdot N_{\text{sideband}}}{N_{\text{prompt}}}, \quad (4.22)$$

where  $N_{\text{prompt}}$  and  $N_{\text{sideband}}$  are the number of events where the reaction time lies within the prompt peak or sideband, respectively.  $w$  is the ratio of the widths of the chosen prompt peak and sideband ranges, see section 3.3. It is now assumed that the random coincidences will exhibit an asymmetry  $\Sigma^{\text{bkg}}$  of their own and are not necessarily described by the detector coefficients  $a$  and  $b$  but rather by  $a^{\text{bkg}}$  and  $b^{\text{bkg}}$ . The probability to detect a prompt peak event  $p_{\text{prompt}}$  and the probability to measure a sideband event  $p_{\text{sideband}}$  are then given by

$$p_{\text{prompt}}(\phi, p_\gamma, |\Sigma, a, b, \Sigma^{\text{bkg}}, a^{\text{bkg}}, b^{\text{bkg}}) = f \cdot \tilde{p}(\phi, p_\gamma | \Sigma, a, b) + (1 - f) \cdot \tilde{p}(\phi, p_\gamma | \Sigma^{\text{bkg}}, a^{\text{bkg}}, b^{\text{bkg}}) \quad (4.23)$$

$$p_{\text{sideband}}(\phi, p_\gamma | \Sigma^{\text{bkg}}, a^{\text{bkg}}, b^{\text{bkg}}) = \tilde{p}(\phi, p_\gamma | \Sigma^{\text{bkg}}, a^{\text{bkg}}, b^{\text{bkg}}). \quad (4.24)$$

If there are  $n$  prompt peak and  $m$  sideband events, the joint likelihood of all events  $\mathcal{L}$  is thus given by

$$\mathcal{L} = \prod_{i=1}^n p_{\text{prompt}}(\phi_i, p_{\gamma,i} | \Sigma, a, b, \Sigma^{\text{bkg}}, a^{\text{bkg}}, b^{\text{bkg}}) \prod_{j=1}^m p_{\text{sideband}}(\phi_j, p_{\gamma,j} | \Sigma^{\text{bkg}}, a^{\text{bkg}}, b^{\text{bkg}}), \quad (4.25)$$

or, equivalently

$$\begin{aligned} \ln \mathcal{L} = & \sum_{i=1}^n \ln p_{\text{prompt}}(\phi_i, p_{\gamma,i} | \Sigma, a, b, \Sigma^{\text{bkg}}, a^{\text{bkg}}, b^{\text{bkg}}) \\ & + \sum_{j=1}^m \ln p_{\text{sideband}}(\phi_j, p_{\gamma,j} | \Sigma^{\text{bkg}}, a^{\text{bkg}}, b^{\text{bkg}}). \end{aligned} \quad (4.26)$$

Again, independency of all data points is essential, when formulating a combined likelihood function this way. Eighteen<sup>6</sup> parameters have to be determined in total, either via a conventional frequentist approach or a BAYESIAN approach to this non-linear fitting problem.

### Frequentist

Best fit estimates can be derived by maximizing the likelihood  $\mathcal{L}$ , or, for computational convenience, by minimizing  $-\ln \mathcal{L}$ . The *ROOT* library [**root**] offers the method *TTree::UnbinnedFit* to perform an unbinned maximum likelihood fit on data filled in a *TTree* [**runbinnedFit**], which was used to perform the fit. Minimization and statistical error calculation are performed by *MINUIT* [**minuit**]. Errors are hereby estimated either symmetrical from the paraboloid shape of  $(-\ln \mathcal{L})$  using the *HESSE* algorithm or asymmetric from the half-maximum values of  $(-\ln \mathcal{L})$  using the *MINOS* algorithm without making assumptions on the shape of the likelihood, if necessary [**minuit**].

### Bayesian

The joint posterior of all fit parameters given the data  $\phi, p_\gamma$  is

$$p(\Sigma, a, b, \Sigma^{\text{bkg}}, a^{\text{bkg}}, b^{\text{bkg}} | \phi, p_\gamma) \propto \mathcal{L}(\phi, p_\gamma | \Sigma, a, b, \Sigma^{\text{bkg}}, a^{\text{bkg}}, b^{\text{bkg}}) \cdot \pi(\Sigma, a, b, \Sigma^{\text{bkg}}, a^{\text{bkg}}, b^{\text{bkg}}), \quad (4.27)$$

where  $\pi(\theta)$  denotes the combined prior of all fit parameters which factors into each individual prior since all parameters are independent:

$$\pi(\Sigma, a, b, \Sigma^{\text{bkg}}, a^{\text{bkg}}, b^{\text{bkg}}) = \pi(\Sigma) \cdot \pi(a) \cdot \pi(b) \cdot \pi(\Sigma^{\text{bkg}}) \cdot \pi(a^{\text{bkg}}) \cdot \pi(b^{\text{bkg}}). \quad (4.28)$$

The priors for  $\Xi \in \{\Sigma, \Sigma^{\text{bkg}}\}$  and  $\xi \in \{a, b, a^{\text{bkg}}, b^{\text{bkg}}\}$  are again chosen non-informative, broadly centered around 0

$$\Xi \sim \mathcal{N}(0, 1)_{[-1, 1]} \quad \xi_k \sim \mathcal{N}(0, 0.1). \quad (4.29)$$

From references [Afz19; Har17] it is expected that  $\xi_k \ll 1$ , therefore the chosen widths of the priors resemble a, relatively speaking, broad distribution.

This model, consisting of the likelihood in Eq. (4.26) and the priors in Eq. (4.29), is implemented in Stan [**stan**], so that samples from the posterior in the physically allowed region ( $\Xi \in [-1, 1]$ ) are again obtained via NUTS [**nuts**].

---

<sup>6</sup> The FOURIER series is constructed such that  $a_0 = 0, b_0 = 1$ .

## 4.2 Determination of $\Sigma_\eta$ using Bayesian statistics

This section will now demonstrate the application of the discussed methods to obtain the beam asymmetry  $\Sigma$  for  $\eta$  photoproduction with selected data provided from reference [Afz19]. For each method only the respective BAYESIAN approach will be used and compared to the results from [Afz19] to confirm that it is a valid method. As an additional sanity check toy Monte Carlo samples are generated and analyzed.

### 4.2.1 Application of methods to toy Monte Carlo data

Although results can be compared to the already accomplished ones in reference [Afz19], verifying the correct functioning of the fitting methods is still useful. This is done by generating events that follow the expected distributions of  $N^{\parallel/\perp}$  with fixed and known parameters. With the simulated event yields the binned and unbinned fit are performed as described previously. Repeating this for a large number of times should reproduce the input parameters if the methods work as intended.

#### Event yield asymmetries

The asymmetry  $A(\phi)$  is built from the event yields  $N^{\parallel/\perp}$ , which are distributed according to

$$N^\parallel = N_0 \left[ 1 - p_\gamma^\parallel \Sigma \cos \left( 2 (\alpha^\parallel - \phi) \right) \right], \quad (4.30)$$

$$N^\perp = N_0 \left[ 1 - p_\gamma^\perp \Sigma \cos \left( 2 (\alpha^\perp - \phi) \right) \right], \quad (4.31)$$

where the parameters are chosen as  $\Sigma = 0.3$ ,  $p_\gamma^\parallel = 0.25$ ,  $p_\gamma^\perp = 0.3$ . In each toy Monte Carlo bin the number of generated samples per setting  $N_{\text{total}}^{\parallel/\perp}$  is given by a Poisson distribution

$$N_{\text{total}}^\parallel \sim \mathcal{P}(800) \quad N_{\text{total}}^\perp \sim \mathcal{P}(1000), \quad (4.32)$$

to simulate the statistics of the  $\gamma p \rightarrow p\eta$  final state as accurately as possible [Afz19]. The samples from the distributions (4.30),(4.31) are drawn using the `TH1::GetRandom` [**rrandom**] function provided by `ROOT` [**root**]. The function from which samples should be drawn is integrated point wise and then normalized. The normalized integral is approximated by a parabola for each bin. A random number between 0 and 1 is generated and assigned to the according bin, where the respective parabola is evaluated to give the desired random value. [**rrandom**]. In total, 10000 toy Monte Carlo bins were simulated and the asymmetry built for 12 bins in  $\phi$ , to conform with the binning chosen in reference [Afz19]. The resulting asymmetry  $A(\phi)$  is shown in Figure 4.2 for several bins as the orange data points with statistical errors according to GAUSSIAN error propagation. Additionally shown is a  $\chi^2$  fit (orange line) to the asymmetry together with posterior predictive checks as obtained from a fully BAYESIAN fit according to the introduced model (blue distributions). This BAYESIAN fit was performed employing  $n_{\text{chain}} = 4$  MARKOV chains with  $n_{\text{samples}} = 1000$  samples each. The warm-up period for each chain has the same length of  $n_{\text{warm up}} = 1000$

$$n_{\text{chain}} = 4 \quad n_{\text{samples}} = 1000 \quad n_{\text{warm up}} = 1000. \quad (4.33)$$

The goodness of fit is checked via the introduced  $p$ -values  $p = T(A_{\text{rep}} > A)$ , and are shown as black points with propagated error bars on the bottom. The optimal value of  $p = 0.5$  is marked by the dashed line and realizes the mean of the distribution of all  $p$ -values, so that one can assume good description of the data by the fits, see Figure 4.3. This replaces the investigation of the  $\chi^2/\text{NDF}$  distribution in the case of a frequentist fit, which should have a mean of 1.

To check whether the fit is unbiased and provides correct error estimation one can investigate the normalized residuals

$$\xi = \frac{\Sigma^{\text{fit}} - \Sigma^{\text{true}}}{\Delta\Sigma^{\text{fit}}} \quad (4.34)$$

in the case of a least-squares fit. Here  $\Sigma^{\text{fit}}$  and  $\Delta\Sigma^{\text{fit}}$  are the value and corresponding statistical error for the beam asymmetry as obtained from the fit and  $\Sigma^{\text{true}}$  is the true value that was used to throw the toy MC experiments. An unbiased fit with right estimation of errors yields [**statistics**]

$$\xi \sim \mathcal{N}(0, 1). \quad (4.35)$$

This criterion obviously cannot be applied in the same way to a **BAYESIAN** fit. The fit results are distributions and therefore lack point estimates  $\Sigma^{\text{fit}}$  and errors  $\Delta\Sigma^{\text{fit}}$ . However, one can modify Equation (4.34) to the needs of a **BAYESIAN** fit to assess its performance:

$$\Xi = \frac{\text{median}(\{\Sigma^{\text{fit}}\}) - \Sigma^{\text{true}}}{\text{std}(\{\Sigma^{\text{fit}}\})} \sim \mathcal{N}(0, 1). \quad (4.36)$$

Instead of the point estimates  $\Sigma^{\text{fit}}$  the median of the set of all draws from the marginal posteriors  $\{\Sigma^{\text{fit}}\}$  is shifted by the true value  $\Sigma^{\text{true}}$  and normalized by the standard deviation as an error estimate for each fit. Although this is not a rigorously derived quantity it allows to identify possible bias if mean ( $\Xi$ )  $\neq 0$ . Furthermore, checking that  $\sigma \approx 1$  will affirm whether the width of the marginal posterior distributions is sensible. Figure 4.4 shows the combined  $\Xi$ -distributions of all fits and the unaltered combined posteriors shifted by the true value. As expected, both distributions are normal as a **GAUSSIAN** fit proves. The width of the marginal posterior distributions can be regarded as sensible since the standard deviation of the  $\Xi$  distribution  $\sigma_\Xi \approx 1$ <sup>7</sup>. This is furthermore confirmed by the fact that  $\{\Sigma^{\text{fit}}\} - \Sigma^{\text{true}} = 0$  within one standard deviation. Yet, the fit results tend to underestimate the beam asymmetry, because both distributions are centered out of their statistical error at  $\mu \pm \Delta\mu < 0$ . This indicates bias towards smaller values of the beam asymmetry. Remarkably, this bias is *not* introduced by the **BAYESIAN** fit, but by the choice of binning and available statistics as an extensive investigation of binned fits (least squares and **BAYESIAN**) to toy Monte Carlo data showed. A detailed discussion thereof is given in appendix B. For now it suffices to note the origin of this bias lies in the choice of binning and is thus inevitable. And, most importantly, the introduced bias is negligible compared to the width of the posterior distributions, so that a binned fit will produce valid fit results in any case. Nevertheless this emphasizes the advantage of unbinned fitting, which is discussed in the next paragraph.

<sup>7</sup> One cannot expect to fulfill Eq. (4.35) exactly, since the errors are after all only estimates that aim to create comparability to the least squares fit.

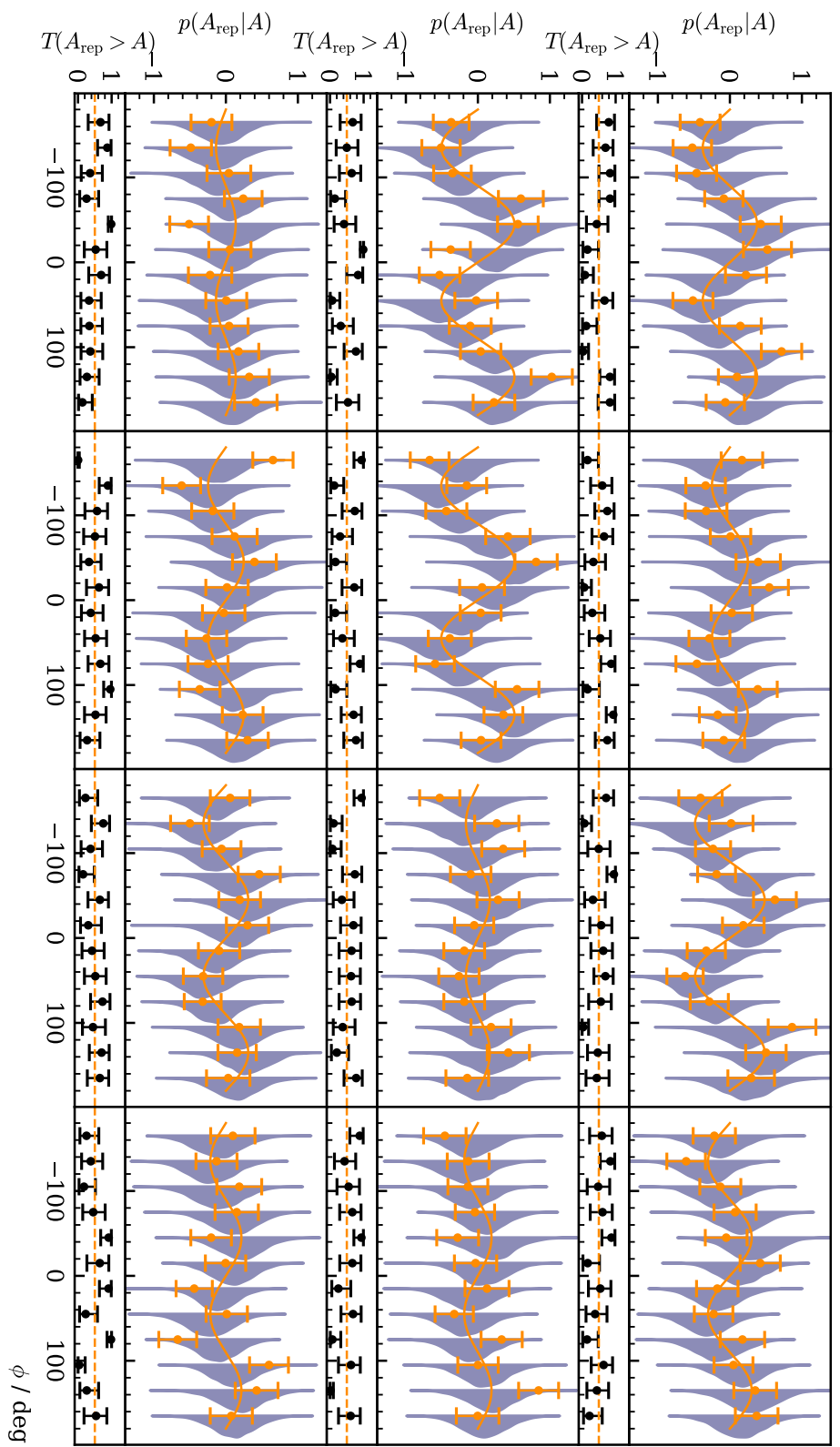


**Figure 4.2:** Posterior predictive checks  $p(A_{\text{rep}}|A)$  from a Bayesian fit to the event yield asymmetries for six toy Monte Carlo bins are shown as distributions. The data points in the upper plot are the asymmetry  $A(\phi)$ , which was additionally fitted using a  $\chi^2$  fit (solid line). The goodness of fit is shown using  $p$ -values, which give the fraction  $T(A_{\text{rep}} > A)$  of replicated samples greater than the original measured value, with propagated statistical error bars on the bottom of each plot. The expected mean value of  $T(A_{\text{rep}} > A) = 0.5$  is indicated by the dashed line.

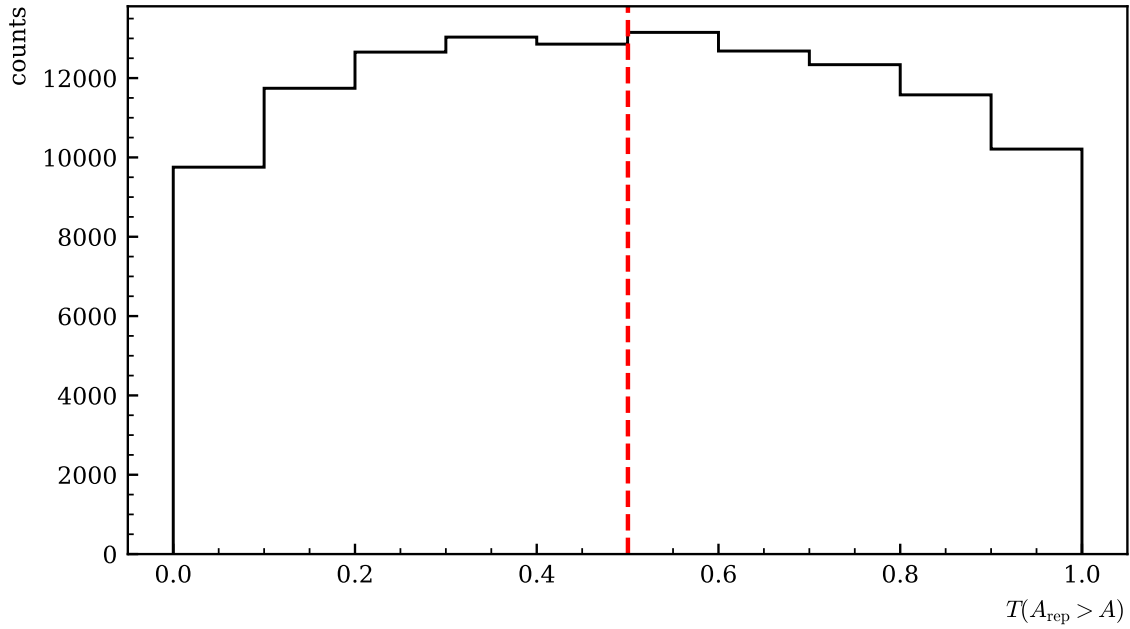


**Figure 4.3:**  $p$  values of all toy Monte Carlo bins. They are centered around their mean at 0.5, which is indicated by the dashed line, and show no bias towards higher or lower values, thus confirming an adequate fit.

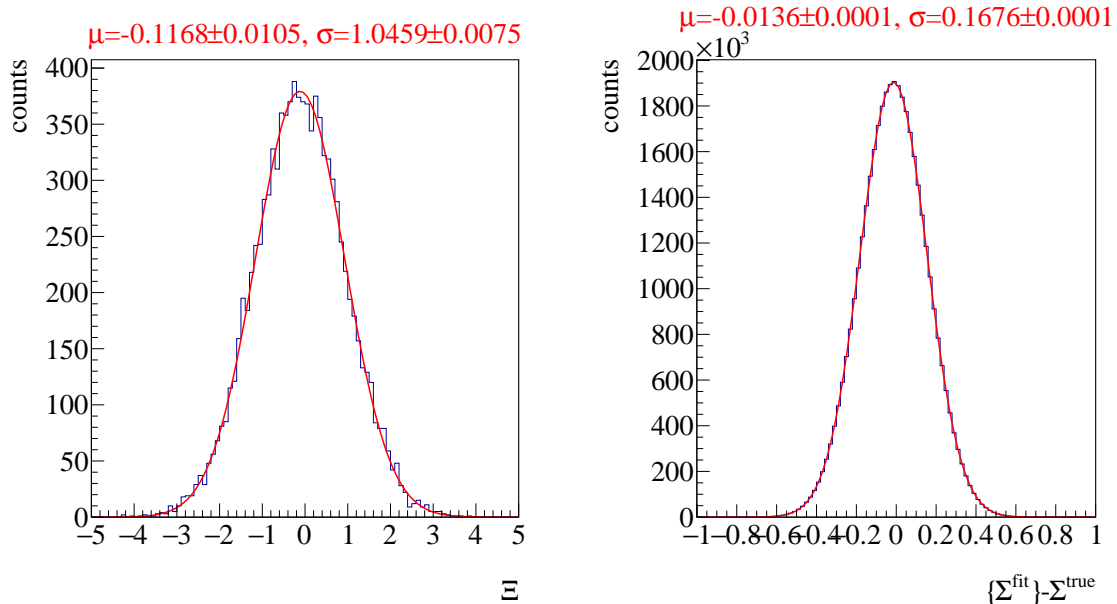


**Figure 4.4:** Left: Combined posterior distributions of all 10000 fits normalized by their respective standard deviation. Right: Unaltered combined posterior distributions of all 10000 fits. A GAUSSIAN fit was performed to determine mean  $\mu$  and standard deviation  $\sigma$  of the distributions with results given on top.

It has been established that the fit produces valid results with sensible statistical errors, i.e. widths of posterior distributions, and the description of the data is in agreement with the expectations. It remains to diagnose the convergence of the MARKOV chains to finally deem the binned fit method appropriate. For this the  $\hat{R}$  value and the relative Monte Carlo standard error (MCSE)  $\frac{\sigma_{\text{MCSE}}}{\text{median}[p(\Sigma|y)]}$  that were introduced in section 1.3 are investigated. If  $\hat{R} < 1.05$  one can assume that the different chains have converged and explored the same parameter space [rhat]. Furthermore the accuracy supplied by the number of draws from the posteriors can be evaluated with the relative MCSE. It is demanded that  $\frac{\sigma_{\text{MCSE}}}{\text{median}[p(\Sigma|y)]} \lesssim 5\%$ . This is the case for 97% of all fits, see Figure 4.5 on the left. When the fit result for the beam asymmetry is close to 0 larger values for the relative MCSE are observed. The  $\hat{R}$  values (Figure 4.5 on the right) clearly indicate good within and between chain convergence. This means that the hyper parameters  $n_{\text{chain}}$ ,  $n_{\text{samples}}$  and  $n_{\text{warm up}}$  as chosen are well tuned, although one may increase the number of sample draws from the posterior for the fit from measured data to further suppress the relative MCSE. Then, only  $11 \cdot 12$  as opposed to 10000 fits have to be performed keeping the computational cost reasonable.

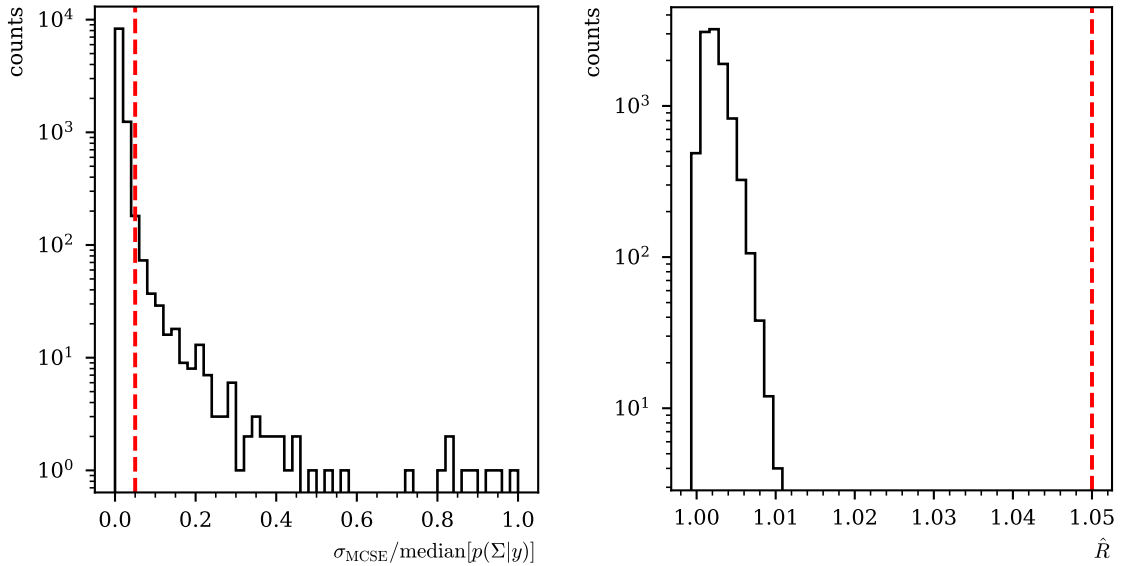


**Figure 4.5:** Left: relative error  $\frac{\sigma_{\text{MCSE}}}{\text{median}[p(\Sigma|y)]}$  Right:  $\hat{R}$  associated with the fit parameter  $\Sigma$ . Both are shown for all 10000 fits. The critical values that should not be exceeded are marked by dashed lines.

### Event based fit

Not only signal events but also contributions from random time background as well as the imperfect detector efficiency  $\epsilon(\phi)$  have to be simulated in order to test the method of event based fitting. For each polarization setting prompt peak and sideband events are drawn from the theoretical  $\phi$ -distributions  $p_{\text{prompt}}$  and  $p_{\text{sideband}}$  which are given in Equations (4.23) and (4.24). The total number of draws per setting and bin is again given by Poisson distributions and the ratio of prompt peak to sideband events is given by the time cut weights  $\{w_i\}_{i=1}^7$  employed for the actual analysis of the  $p\eta$  final state data [Afz19]. This means that seven times prompt peak and sideband events need to be simulated. The

fraction of background events within the prompt peak  $f$  was set to  $f = 0.95$ . Further, the values  $p_\gamma^\parallel = 0.25$ ,  $p_\gamma^\perp = 0.3$ ,  $\Sigma = 0.5$ ,  $\Sigma^{\text{bkg}} = -0.5$  and lastly, a random efficiency function as already chosen in reference [Afz19] were appointed. Finally the hyperparameters  $n_{\text{chain}}$ ,  $n_{\text{samples}}$ ,  $n_{\text{warm up}}$  are chosen the same as previously. Table 4.1 shows a summary of all toy Monte Carlo properties. In total, 1000

<b>chosen parameters</b>	$p_\gamma^\parallel = 0.25$ , $p_\gamma^\perp = 0.3$ , $\Sigma = 0.5$ , $\Sigma^{\text{bkg}} = -0.5$ , $f = 0.95$ , $w_1 = \frac{15}{210}$ , $w_2 = \frac{8}{210}$ , $w_3 = \frac{4}{210}$ , $w_4 = \frac{10}{210}$ , $w_5 = \frac{14}{210}$ , $w_6 = \frac{6}{210}$ , $w_7 = \frac{11}{210}$
<b>simulation draws</b>	$7 \cdot N_{\text{total},i}^\parallel \sim \mathcal{P}(800)$ , $7 \cdot N_{\text{total},i}^\perp \sim \mathcal{P}(1000)$ $ _{i=1}^7$
	signal in prompt      background in prompt      sideband
	$N_{\text{total}}^{\parallel/\perp} \cdot f$ $N_{\text{total}}^{\parallel/\perp} \cdot (1-f)$ $N_{\text{total}}^{\parallel/\perp} \cdot (1-f) \cdot 1/w_i$
<b>efficiency function</b>	$\epsilon(\phi) = 1/10.5 \cdot (9.3 + 0.28 \cdot \cos \phi + 0.24 \cdot \sin 3\phi)$
<b>hyperparameters</b>	$n_{\text{samples}} = 1000$ , $n_{\text{chain}} = 4$ , $n_{\text{warm up}} = 1000$

**Table 4.1:** Summary of the complete setting of all toy Monte Carlo experiments for the event based fit. Values and table layout adapted from [Afz19].

toy Monte Carlo experiments are thrown. To evaluate the fit results only the posterior distributions are available. As before, the residuals  $\Xi$  are built from all fits, now for  $\Sigma$  as well as  $\Sigma^{\text{bkg}}$ . They are shown in Figure 4.6 together with the unnormalized posterior distributions. Note that the distributions are truncated towards the tails at  $\Sigma \rightarrow 1$  and  $\Sigma^{\text{bkg}} \rightarrow -1$  as implemented in the BAYESIAN fit in Stan. Also the event based fit is able to reproduce the true values within one standard deviation of the posterior distribution  $\sigma_{\text{posterior}}$ . Only slight bias towards smaller values of the signal beam asymmetry is seen, but again with negligible effect on the results in comparison to the widths of the distributions. Additionally, the mean of the distributions are 0 within  $3\sigma$  of their statistical error and the errors are estimated correctly, since  $\sigma_{\text{posterior}} = 1$  within the statistical error. Note that the background beam asymmetry is estimated closer to its true value than the signal beam asymmetry because there are more random background events than signal events.

If the total amount of posterior distributions is not too large one might also combine them in a *pooled likelihood* approach (see subsection 1.3.3). This is shown in Figure 4.7 for both determined asymmetries. Because the true asymmetries are within  $1\sigma$  of the resulting distribution one can finally conclude that the event based fit estimates positions and widths of the posterior distributions correctly.

A check of the relative MCSE and  $\hat{R}$  values as shown in Figure 4.8 reveals also that the hyperparameters  $n_{\text{chain}}$ ,  $n_{\text{samples}}$ ,  $n_{\text{warm up}}$  are correctly tuned. It is noteworthy that the event based fit creates more precise results although less Monte Carlo experiments in total were performed than for the binned fit.

Next to signal and background beam asymmetry the fit also estimates an efficiency function  $\epsilon(\phi)$  that is described by a FOURIER series. The polarization weighted sum of event yields allows to confirm whether a good description of the efficiency is achieved because it is given by the efficiency function modulated only by a constant, see previous section 4.1  $\alpha \tilde{N}^\parallel + \beta \tilde{N}^\perp = c \cdot \epsilon(\phi)$ . Figure 4.9 shows the weighted sum of event yields with the same binning as used in the binned fit together with a posterior predictive check using the draws of all parameters distributions  $a, b$ . As opposed to the binned fit it is

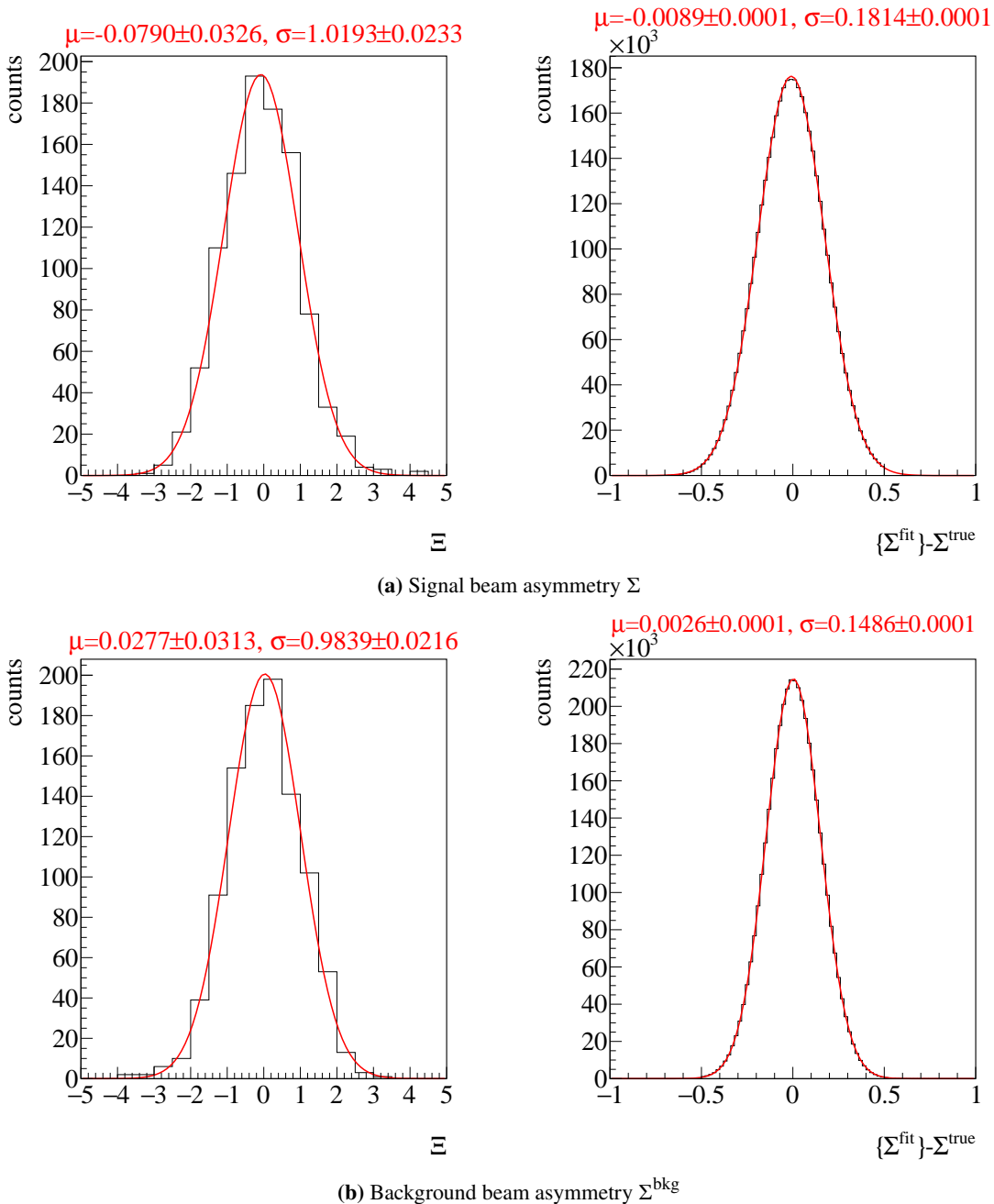


**Figure 4.6:** Combined posteriors for the beam asymmetries  $\Sigma$  and  $\Sigma^{\text{bkg}}$  from all 1000 event based fits. Left: Residuals  $\Xi$  Right: Unnormalized posterior distributions. A GAUSSIAN fit is performed on the distributions with results for mean  $\mu$  and standard deviation  $\sigma$  on top.

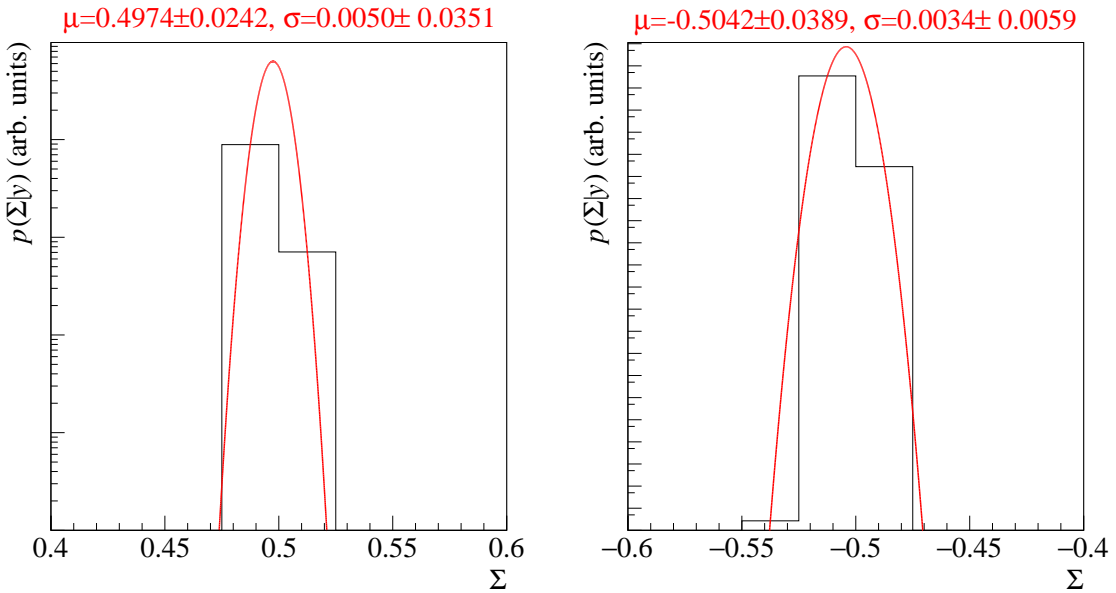


**Figure 4.7:** Combined posterior probabilities using the *pooled likelihood* approach. Left: Signal beam asymmetry, Right: background beam asymmetry. Mean and standard deviation as obtained from a Gaussian fit are shown on top

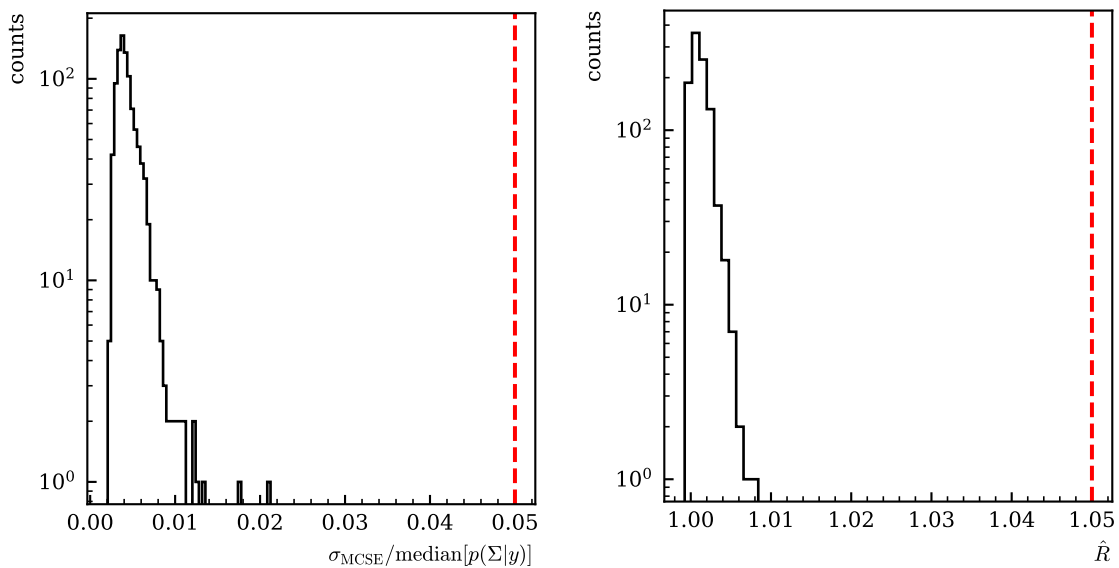


**Figure 4.8:** Left: relative error  $\frac{\sigma_{\text{MCE}}}{\text{median}[p(\Sigma|y)]}$ . Right:  $\hat{R}$  associated with the fit parameter  $\Sigma$ . Both are shown for all 1000 fits. The critical values that should not be exceeded are marked by dashed lines.

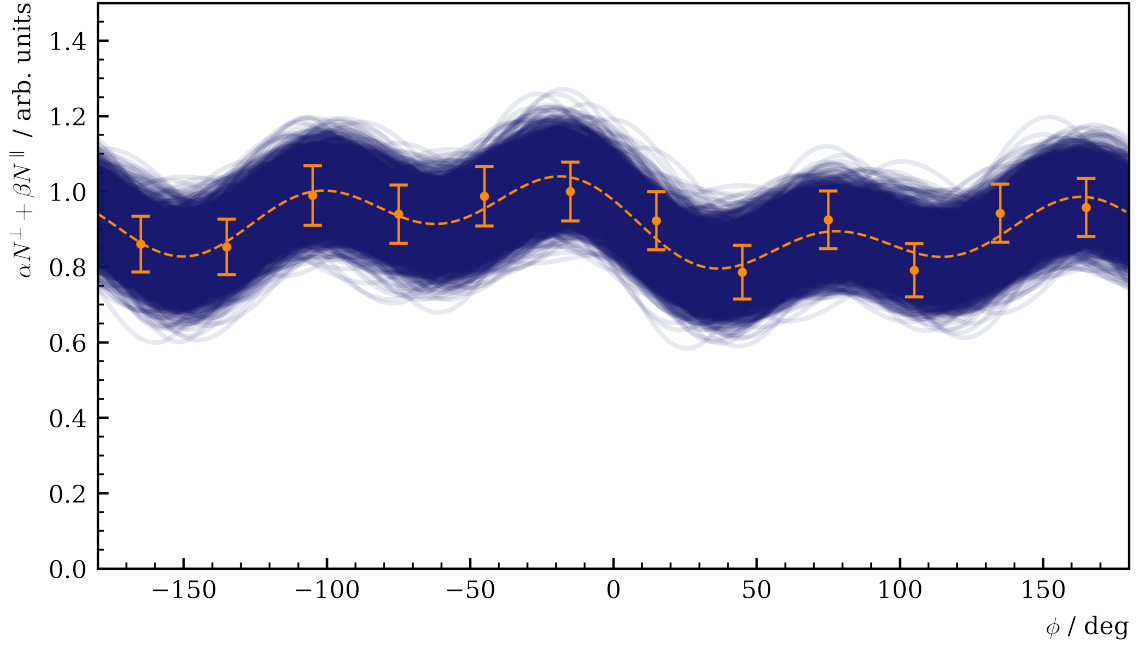


**Figure 4.9:** Posterior predictive check using the draws of the detector coefficients  $a$  and  $b$ . Points with error bars are the polarization weighted sum of event yields. The dashed line is the mean of the predictive values while the solid opaque lines are representative of one simulation draw  $a^{(s)}, b^{(s)}$ .

not only performed at each data point but for significantly more points. This mimics a continuous function as is appropriate for an unbinned fit. However, for better visibility the posterior predictive distributions are not built at every point but the efficiency function is plotted for each set of draws  $a^{(s)}, b^{(s)}, s = 1 \dots 4000$ . No  $p$  values are estimated since they would not be representative of the whole fit. The mean of the posterior predictive distributions is given by the dashed line and agrees within statistical error bars with the simulated data.

### 4.2.2 Application of methods to data

Since both methods were tested successfully using toy Monte Carlo data, both are subsequently applied to real data to extract the beam asymmetry. Since the number of fits is small compared to the amount of fits performed during testing, the amount of posterior draws was increased to 5000 per chain. All other hyperparameters were left the same

$$n_{\text{samples}} = 5000 \quad n_{\text{chain}} = 4 \quad n_{\text{warm up}} = 1000. \quad (4.37)$$

#### Event yield asymmetries

In all bins of beam energy and meson polar angle the binned fit was performed. Similar to the Monte Carlo samples, 12 bins in phi are built to comply with the binning in reference [Afz19], and guarantee comparability.

Figure 4.10 shows the resulting asymmetry  $A(\phi)$  for all angular bins for the energy bin  $1250 \text{ MeV} \leq E_\gamma < 1310 \text{ MeV}$  as orange data points with statistical error bars. Additionally shown is a  $\chi^2$  fit (orange line) to the asymmetry together with posterior predictive checks as obtained from a fully BAYESIAN fit according to the introduced model (blue distributions). The goodness of fit is checked via the introduced  $p$ -values  $p = T(A_{\text{rep}} > A)$ , and are shown as black points with propagated error bars on the bottom. The optimal value of  $p = 0.5$  is marked by the dashed line and realizes the mean of the distribution of all  $p$ -values, so that one can assume good description of the data by the fits, see Figure 4.11. This replaces the investigation of the  $\chi^2/\text{NDF}$  distribution in the case of a frequentist fit.

The MCMC diagnostics reveal that all MARKOV chains have converged and explored the available parameter space completely which is characterized by  $\widehat{R} = 1.00$  for all fits. The increment of posterior draws removed any fluctuations in the  $\widehat{R}$  value that was present before. The relative MCSE is below the (self-)defined threshold of  $\frac{\sigma_{\text{MCSE}}}{\text{median}[p(\Sigma|y)]} < 5\%$  for 95% of all fits. The remaining 5% are fits that estimated the beam asymmetry close to 0 such that further incrementing the number of posterior draws will not amend this. Both, relative MCSE and  $\widehat{R}$  associated with the fit parameter  $\Sigma$  of the binned fit, are shown in Figure 4.12. Thus, one can conclude the successful tuning of hyperparameters concerning the BAYESIAN fit.

#### Event based fit

The discussed BAYESIAN event based fit is also performed for all kinematic bins. The MCMC diagnostics reveal good choice of hyperparameters, as Figure 4.13 shows. As already observed during the toy Monte Carlo experiments, the unbinned fit produces more precise results; 98% of all fits exhibit an MCSE below threshold, those bins with error above threshold are again explained by values of the beam asymmetry  $\Sigma \approx 0$ . Good within and between chain convergence is reached, as  $\widehat{R} = 1.00$  for all fits shows.

The only illustrative measure regarding the performance of the unbinned fit is the posterior predictive distribution of the detector coefficients  $a, b$ . Figure 4.14 shows the weighted sum of event yields with the same binning as used in the binned fit together with a posterior predictive check using the draws of all parameters distributions  $a, b$  for the kinematic bin  $1250 \text{ MeV} \leq E_\gamma < 1310 \text{ MeV}, 0 \leq \cos \theta < 0.17$ . As opposed to the binned fit it is not only performed at each data point but for significantly more points. This mimics a continuous function as is appropriate for an unbinned fit. However, for better visibility the posterior predictive distributions are not built at every point but the efficiency function is

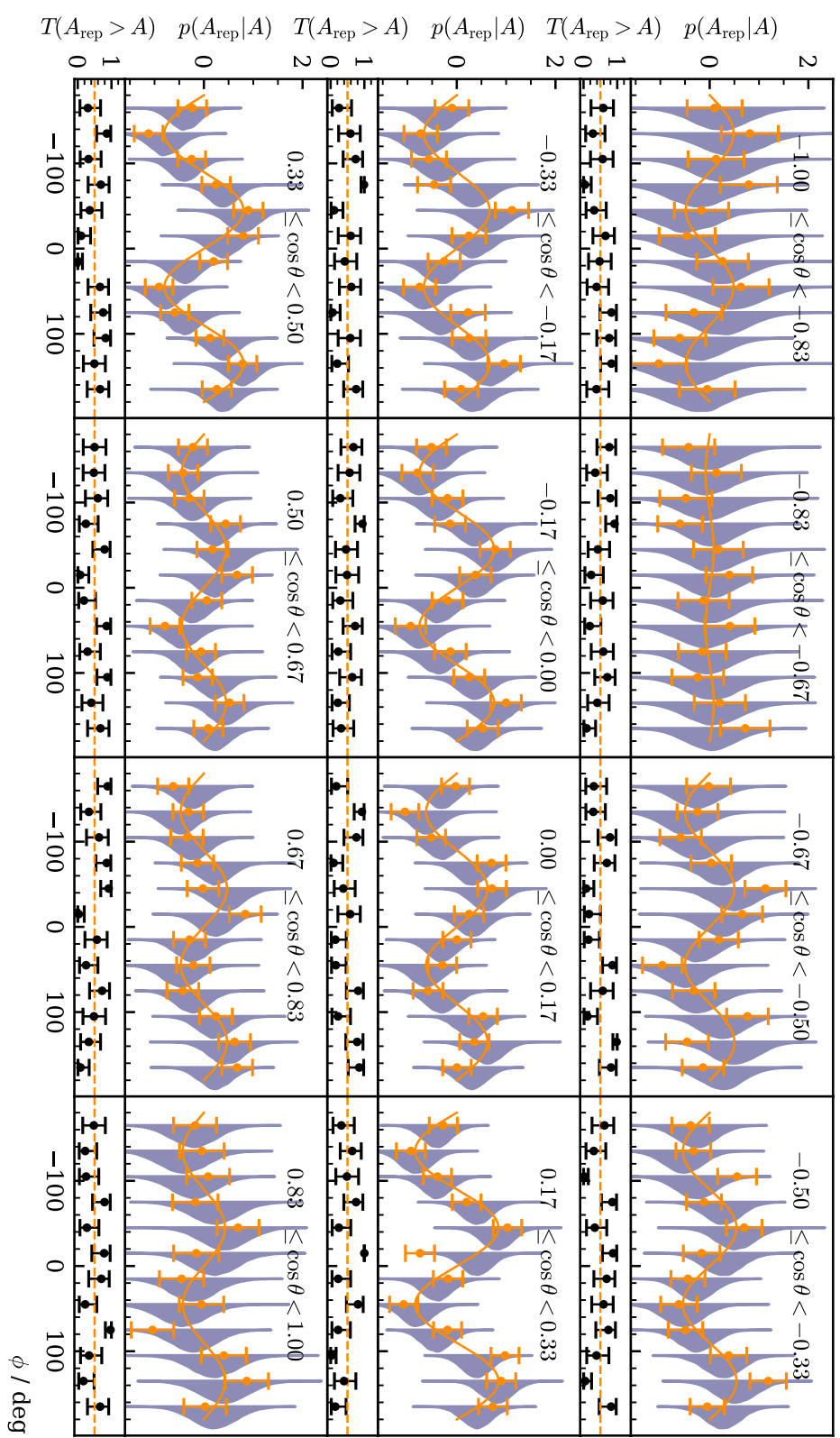


**Figure 4.10:** Posterior predictive checks  $p(A_{\text{rep}}|A)$  from a BAYESIAN fit to the event yield asymmetries for all angular bins of the energy bin  $1250 \text{ MeV} \leq E_\gamma < 1310 \text{ MeV}$ . The data points in the upper plot are the asymmetry  $A(\phi)$ , which was additionally fitted using a  $\chi^2$  fit (solid line). The goodness of fit is shown using  $p$ -values, which give the fraction  $T(A_{\text{rep}} > A)$  of replicated samples greater than the original measured value, with propagated statistical error bars on the bottom of each plot. The expected mean value of  $T(A_{\text{rep}} > A) = 0.5$  is indicated by the dashed line.

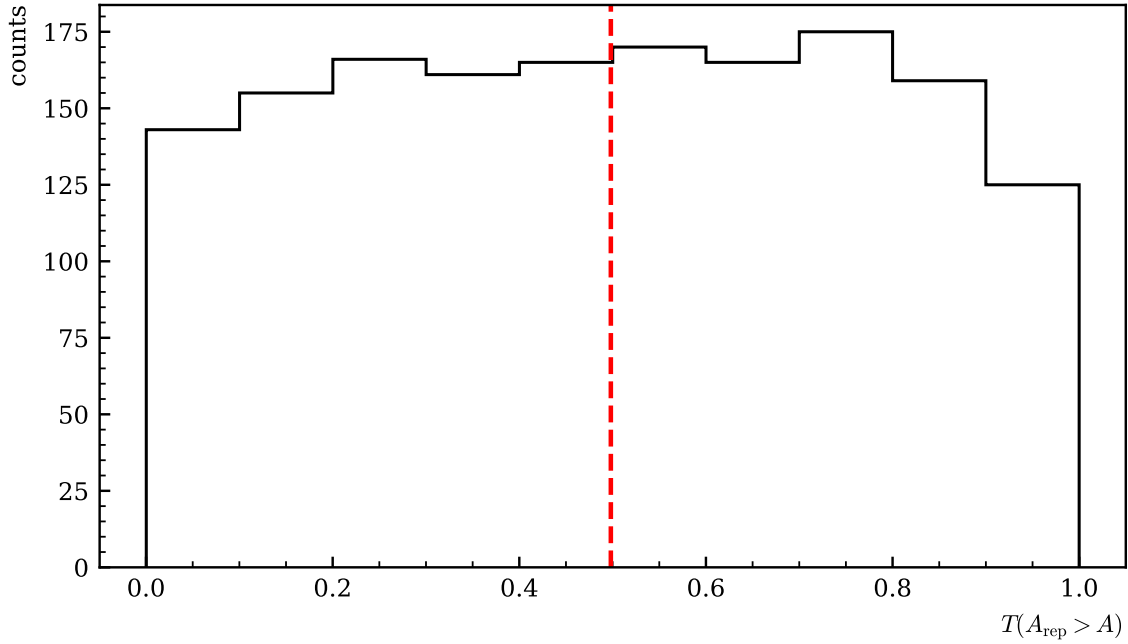


**Figure 4.11:**  $p$  values generated using all fits. They are centered around their mean at 0.5, which is indicated by the dashed line, and show no bias towards higher or lower values, thus confirming an adequate fit.

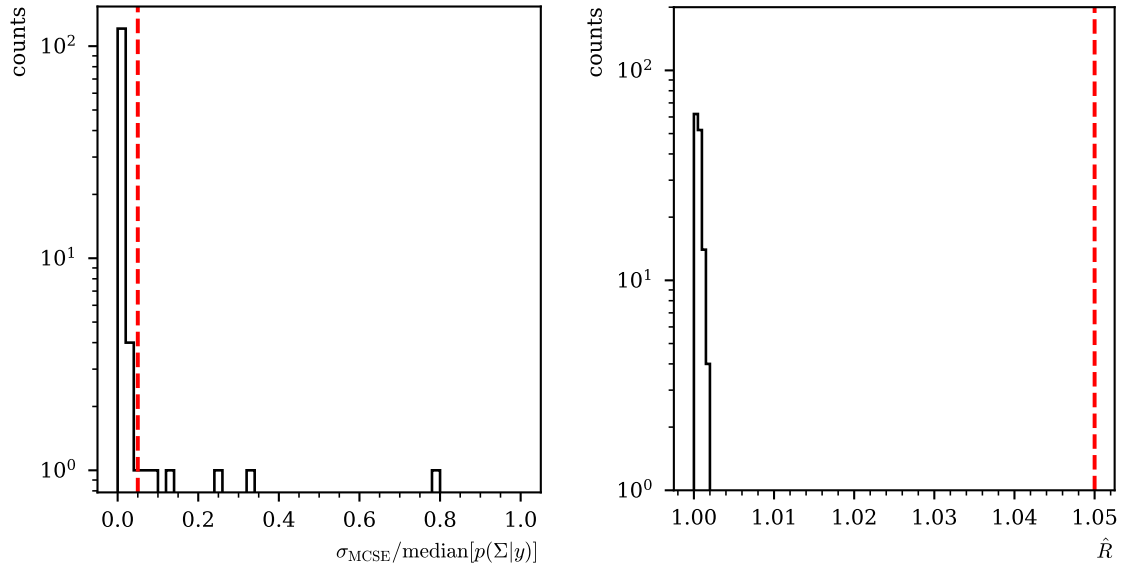


**Figure 4.12:** Left: relative error  $\frac{\sigma_{\text{MCSE}}}{\text{median}[p(\Sigma|y)]}$  Right:  $\hat{R}$  associated with the fit parameter  $\Sigma$ . Both are shown for all  $11 \cdot 12$  binned fits to the asymmetry  $A(\phi)$ . The critical values that should not be exceeded are marked by dashed lines.

plotted for each set of draws  $a^{(s)}, b^{(s)}$ ,  $s = 1 \dots 20000$ . No  $p$  values are estimated since they would not be representative of the whole fit. Note that the detector efficiency  $\epsilon(\phi)$  is almost flat as opposed to the simulated efficiency in subsection 4.2.1. This is an overall observation and not specific to the shown kinematic bin and further confirmed by the fact that the sums of all fit coefficients  $a, b$  are distributed around zero. Regardless of the significance of detection inefficiencies the unbinned fit is nevertheless able to obtain good agreement between fit and data; the mean of all posterior predictive distributions (dashed line) agrees within statistical error bars with the data points.

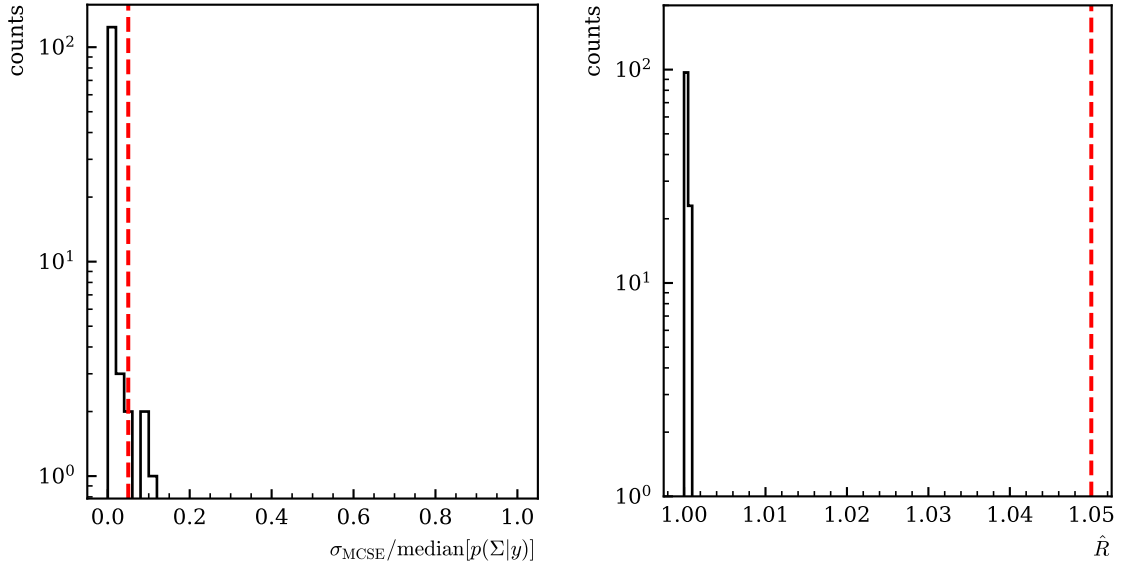


**Figure 4.13:** Left: relative error  $\frac{\sigma_{MCSE}}{\text{median}[p(\Sigma|y)]}$  Right:  $\hat{R}$  associated with the fit parameter  $\Sigma$ . Both are shown for all  $11 \cdot 12$  unbinned fits. The critical values that should not be exceeded are marked by dashed lines.

### 4.2.3 Discussion

The final results for the beam asymmetry obtained with both methods are shown in Figure 4.15 for all bins in beam energy and meson polar angle. Along with the marginal posterior distributions obtained from both introduced methods point estimates from a  $\chi^2$  fit and an unbinned fit [Afz19] are shown. An important intermediate result is that all results agree with each other within statistical error bars or within the width of the marginal posterior distributions. Any effects that lead to slightly distinguishable point estimates from a binned or unbinned fit are propagated directly throughout the BAYESIAN fit; then each distribution is centered around the point estimate of the respective fitting method. The results from the binned and unbinned fit with error bars on average cover 68% of the respective marginal posterior distributions, corresponding to a  $1\sigma$  interval. Thus, in general, the application of BAYESIAN methods has proven to give the same results and no systematic error is introduced by the BAYESIAN approach.

The effort of implementing the binned or unbinned fit in a BAYESIAN approach is comparable to using standard libraries provided by e.g. *python* [**python**] or *ROOT* [**root**]. Due to the probabilistic structure of the Stan language [**stan**] implementation of likelihood and prior models is straightforward

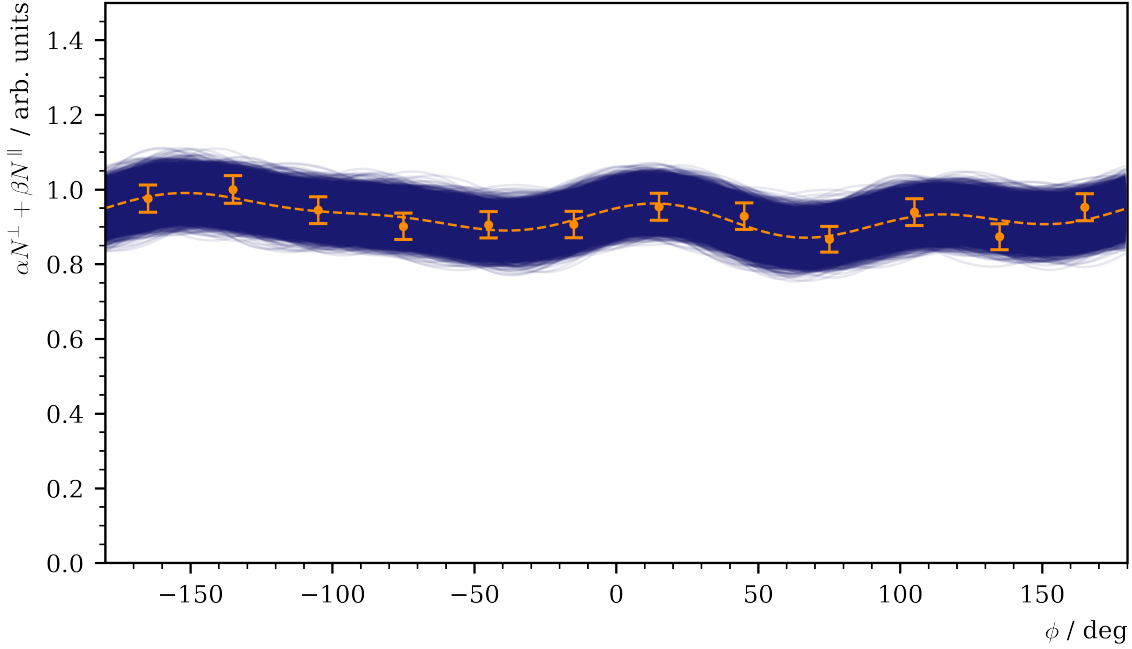


**Figure 4.14:** Posterior predictive check using the draws of the detector coefficients  $a$  and  $b$  for the kinematic bin  $1250 \text{ MeV} \leq E_\gamma < 1310 \text{ MeV}$ ,  $0 \leq \cos \theta < 0.17$ . Points with error bars are the polarization weighted sum of event yields. The dashed line is the mean of the predictive values while the solid opaque lines are representative of one simulation draw  $a^{(s)}, b^{(s)}$ .

and the sampling algorithms can be accessed or modified to ones needs intuitively. However, the BAYESIAN fit requires more careful preparation and also diagnostics. On one hand, the choice of priors has to be made. On the other hand, the fitting procedure is inherently different; not only the goodness of fit compared with data has to be checked but also the convergence of the MARKOV chains themselves.

The computational cost also increases greatly in comparison to the traditional frequentist approaches. Especially the unbinned BAYESIAN fit requires a lot of computation time, where the number of data points is of order  $O(10^4)$  as opposed to 12 data points for the binned fit. This can be understood considering the underlying algorithms; the least squares fit and also the unbinned maximum likelihood fit both aim to minimize a given test statistic which is achievable by (numeric) differentiation. Determining marginal posterior distributions from BAYESIAN inference on the other hand requires (numeric) integration, making it the more complex task which is observable in the consumed computation time.

Yet, the additional effort is rewarded by the fact that the BAYESIAN fit will yield *distributions* for all parameters as opposed to point estimates with error bars. This is especially useful for polarization observables which may be used as input for PWA calculations. Here error estimates can be derived from the distributions e.g. as (multiple) standard deviations, the full width at half maximum or similar. If furthermore a BAYESIAN approach is pursued, also the whole distributions may be used. Because the final results are distributions also the structure of these may be analyzed uncovering possible multimodalities as well as distributions differing from i.e. a symmetric GAUSSIAN. Another advantage

of the BAYESIAN fit is the ability to truncate the posterior samples to the relevant or allowed parameter space. In the very first energy bin in Figure 4.15 this is visible clearly where several point estimates exceed the physical limit of  $\Sigma = 1$  as opposed to the obtained marginal posteriors. Lastly, the BAYESIAN fit allows much more flexible changes to the fitted model, as will be discussed in the next section 4.3.

### 4.3 Determination of $\Sigma_{\eta'}$

After successfully testing the application of BAYESIAN methods this section will demonstrate the extraction of new results for the beam asymmetry in  $\eta'$  photoproduction off the proton obtained at the CBELSA/TAPS experiment. Only the event based fitting method is applied and the binned fitting of event yield asymmetries is discarded because on one hand the available statistics will on average give only few counts per bin  $(E_\gamma, \cos \theta, \phi)$  of order  $\mathcal{O}(10^1)$ , depending on the specific number of  $\phi$ -bins. This will result in very large statistical errors per bin. On the other hand this could be compensated by choosing fewer bins in  $\phi$  which would however amplify the systematic underestimation of the beam asymmetry which is discussed in appendix B.

The event based fits are performed as unbinned maximum likelihood fit and as BAYESIAN fit. New toy Monte Carlo experiments are thrown adapting to the significantly decreased statistics. Also, tests regarding the background contamination of Monte Carlo samples are made.

#### 4.3.1 Application of event based fit to toy Monte Carlo data

After selecting all suitable event candidates for  $\gamma p \rightarrow p\eta' \rightarrow p\gamma\gamma$  reactions there still remain significant background contributions which make up roughly 20% of all events averaged over all kinematic bins. Investigation of Monte Carlo simulations of different mesonic final states revealed they are mainly realized by the false reconstruction of  $2\pi^0$  photoproduction events (see chapter 3). It was thus investigated how the presence of two beam asymmetries  $\Sigma_1$  and  $\Sigma_2$  affects the fit. The combined differential cross section is then given by

$$\frac{d\sigma}{d\Omega_{\text{pol}}}(\phi) = \frac{d\sigma^{(1)}}{d\Omega_{\text{pol}}}(\phi) + \frac{d\sigma^{(2)}}{d\Omega_{\text{pol}}}(\phi) \quad (4.38)$$

$$= \frac{d\sigma^{(1)}}{d\Omega_0} \cdot \left(1 - p_\gamma \Sigma_1 \cos(2\phi)\right) + \frac{d\sigma^{(2)}}{d\Omega_0} \cdot \left(1 - p_\gamma \Sigma_2 \cos(2\phi)\right). \quad (4.39)$$

If now the fraction  $\delta$  of events in the final state with beam asymmetry  $\Sigma_2$  is known one can express the unpolarized cross sections via a common combined unpolarized cross section as

$$\frac{d\sigma^{(1)}}{d\Omega_0} = (1 - \delta) \cdot \frac{d\sigma}{d\Omega_0} \quad \frac{d\sigma^{(2)}}{d\Omega_0} = \delta \cdot \frac{d\sigma}{d\Omega_0}. \quad (4.40)$$

Plugging Equation (4.40) into Equation (4.39) then yields

$$\frac{d\sigma}{d\Omega_{\text{pol}}}(\phi) = \frac{d\sigma}{d\Omega_0} \cdot \left(1 - p_\gamma [(1 - \delta) \cdot \Sigma_1 + \delta \cdot \Sigma_2] \cos(2\phi)\right). \quad (4.41)$$

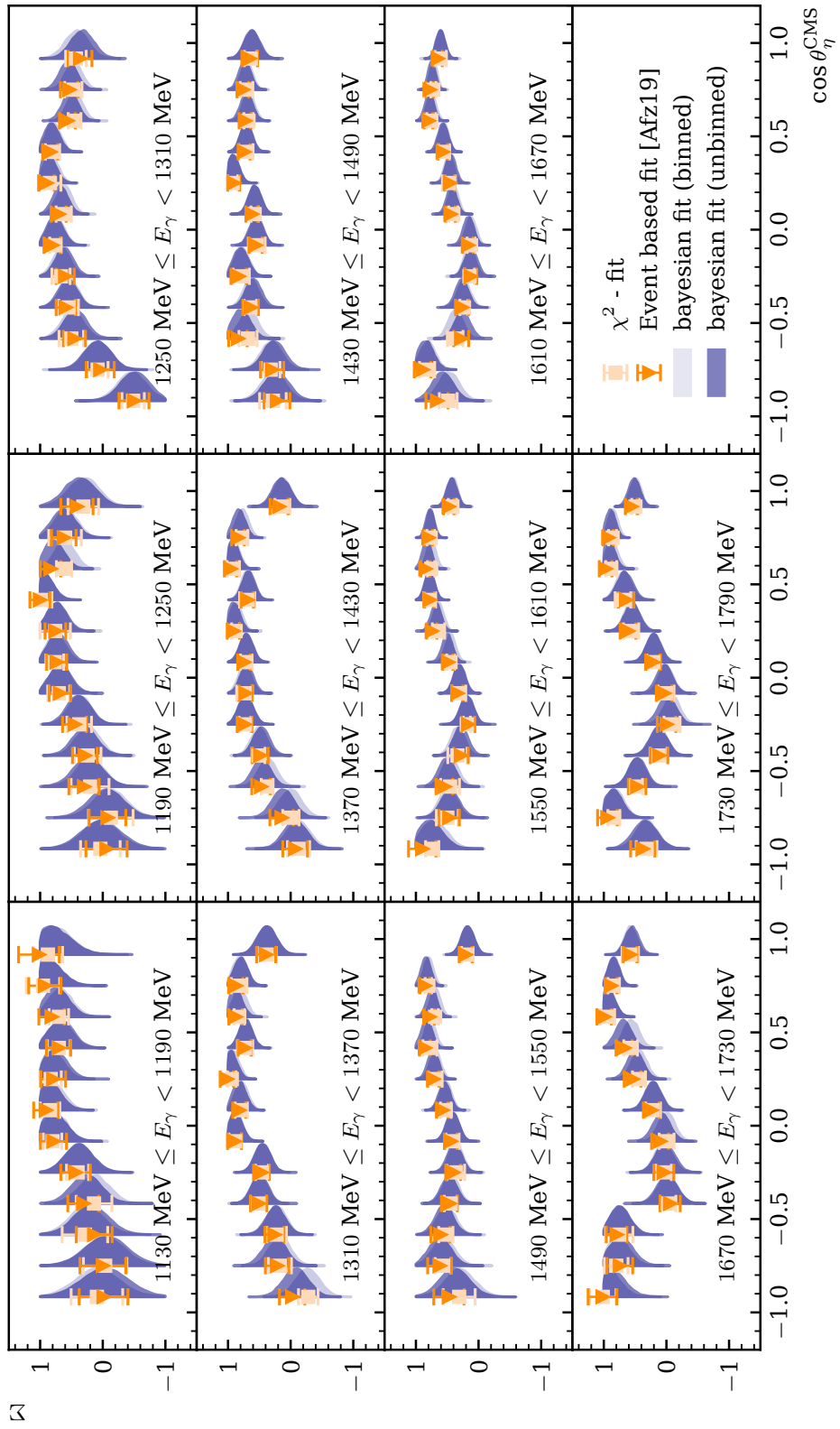


**Figure 4.15:** Final results for the beam asymmetry  $\Sigma$  in  $\eta$  photoproduction off the proton for all kinematic bins obtained with BAYESIAN methods. They are compared with the results of a least squares fit and an unbinned fit as given in reference [Afz19]. All results agree within statistical error bars or within the widths of marginal posterior distributions.

In the presence of background  $\Sigma^{\text{bkg}}$ <sup>8</sup> all measured values for the beam asymmetry  $\Sigma^{\text{meas}}$  are systematically shifted from their true value  $\Sigma^{\text{true}}$ , depending on the amount of background, if the methods described in section 4.1 are used without modification, i.e.

$$\Sigma^{\text{meas}} = (1 - \delta) \cdot \Sigma^{\text{true}} + \delta \cdot \Sigma^{\text{bkg}}. \quad (4.42)$$

This is an important intermediate result: If the background asymmetry  $\Sigma^{\text{bkg}}$  and the corresponding fraction of events  $\delta$  that exhibit this asymmetry are known, the true values  $\Sigma^{\text{true}}$  can be obtained. If  $\Sigma^{\text{bkg}}$  is not known this is a source of systematic error.

Table 4.2 shows all characteristics of the investigated toy Monte Carlo experiments, the values for polarization and statistics per bin were chosen to match the respective average values in the selected data for the  $\gamma p \rightarrow p\eta' \rightarrow p\gamma\gamma$  final state. Furthermore  $\delta = 20\%$  of all events were simulated as background with beam asymmetry  $\Sigma_2$  while the remainder of events is simulated with beam asymmetry  $\Sigma_1$ . The amount of random time background in the prompt peak is set to  $(1 - f) = 0.05$  while the sideband events are weighted by  $w = \frac{13}{200}$  (see section 3.3). The same efficiency function and hyperparameters as previously are employed with the exception of the number of posterior draws which is raised to  $n_{\text{samples}} = 5000$  from the beginning. Because of the smaller amount of data this does not increase the computational cost irrationally.

<b>chosen parameters</b>	$p_\gamma^\parallel = 0.3, p_\gamma^\perp = 0.3, \Sigma_1 = 0.5, \Sigma_2 = -0.3, \Sigma_t^{\text{bkg}} = -0.5, f = 0.95, \delta = 0.2$ $w = \frac{13}{200}$
<b>simulation draws</b>	$N_{\text{total}}^{\parallel} \sim \mathcal{P}(200), N_{\text{total}}^{\perp} \sim \mathcal{P}(200)$
	signal in prompt      background in prompt      sideband $N_{\text{total}}^{\parallel/\perp} \cdot f$ $N_{\text{total}}^{\parallel/\perp} \cdot (1 - f)$ $N_{\text{total}}^{\parallel/\perp} \cdot (1 - f) \cdot 1/w$
<b>efficiency function</b>	$\epsilon(\phi) = 1/10.5 \cdot (9.3 + 0.28 \cdot \cos \phi + 0.24 \cdot \sin 3\phi)$
<b>hyperparameters</b>	$n_{\text{samples}} = 5000, n_{\text{chain}} = 4, n_{\text{warm up}} = 1000$

**Table 4.2:** Summary of the complete setting of all toy Monte Carlo experiments for the event based fit. Table layout adapted from [Afz19].

### Unbinned maximum likelihood fit

To test the unbinned maximum likelihood fit and its response to the presence of background, 10000 toy Monte Carlo bins are created according to table 4.2. The expected beam asymmetry is

$$\Sigma^{\text{meas}} = 0.8 \cdot 0.5 - 0.2 \cdot 0.3 = 0.34. \quad (4.43)$$

Building the normalized residuals with respect to  $\Sigma^{\text{meas}}$  and the random time background asymmetry  $\Sigma_t^{\text{bkg}}$  yields standard normal distributions, see Figures 4.16 and 4.17, thus fulfilling the expectations

<sup>8</sup> For clarity, the beam asymmetry associated with random time background will in this section be denoted as  $\Sigma_t^{\text{bkg}}$  and the beam asymmetry associated with background reactions as  $\Sigma^{\text{bkg}}$ .

entirely. This allows Equation (4.42) to be applied on results obtained with this method provided the background beam asymmetry is known. Any errors on  $\Sigma^{\text{bkg}}$  may be propagated in a GAUSSIAN manner. The beam asymmetry is estimated without bias and the errors are correctly estimated as confirmed by  $\mu = 0$  and  $\sigma = 1$  for the normalized residuals within few widths of the statistical errors. Note that the unnormalized distributions are significantly broader than the ones examined in the previous section which is due to the decreased statistics in each bin which already indicates larger statistical errors. The decreased statistics also cause greater variation in the fitted efficiency function that is seen in Figure 4.18, which still describes the data very well.

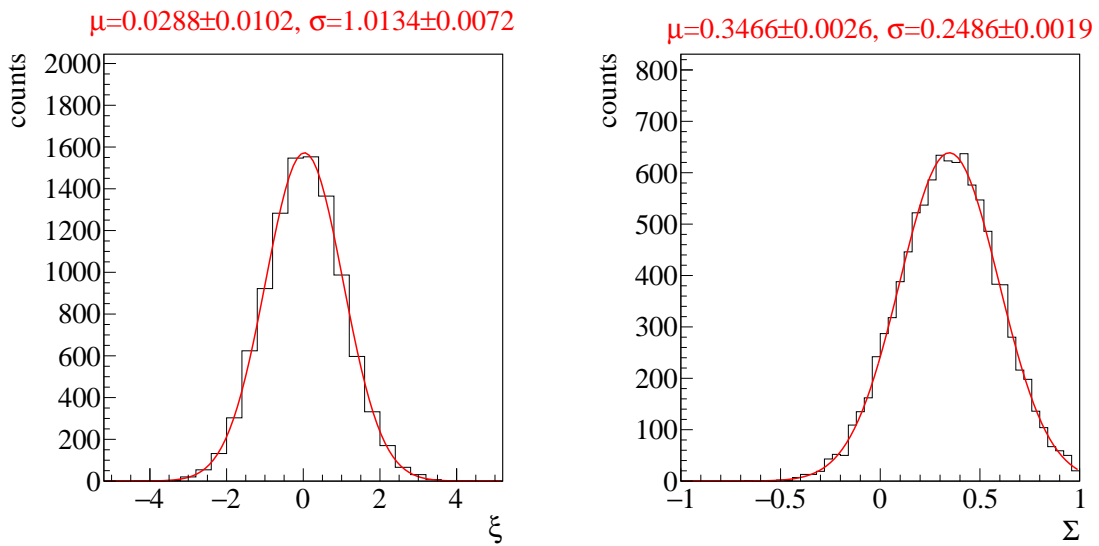


**Figure 4.16:** Normalized residuals (left) and unaltered distribution (right) of all 10000 fits for the beam asymmetry  $\Sigma = (1 - \delta) \cdot \Sigma_1 + \delta \cdot \Sigma_2$ . GAUSSIAN fits are performed with results given on top of each plot.

### Unbinned BAYESIAN fit

When performing a BAYESIAN fit a systematic shift like Equation (4.42) as result of background contributions is not easily applicable. The posterior distributions may be shifted by a constant value but including statistical errors of the background beam asymmetry is not possible. To circumvent this, the background beam asymmetry can be included inherently in the likelihood function that is part of the model being fitted. In practice,  $\delta$  and  $\Sigma_2$  have to be part of the data that is fed into the probabilistic model. In general though  $\Sigma_2$  will have a statistical error, which can be included in the fashion of modeling *missing data [stan]*. Doing so, the value for  $\Sigma_2$  is regarded as an estimate for the true, unknown (or missing) value  $\Sigma_2^{\text{true}}$ . The statistical error  $\tau$  of  $\Sigma_2$  specifies the measurement model assuming GAUSSIAN errors

$$\Sigma_2^{\text{true}} \sim \mathcal{N}(\Sigma_2, \tau). \quad (4.44)$$

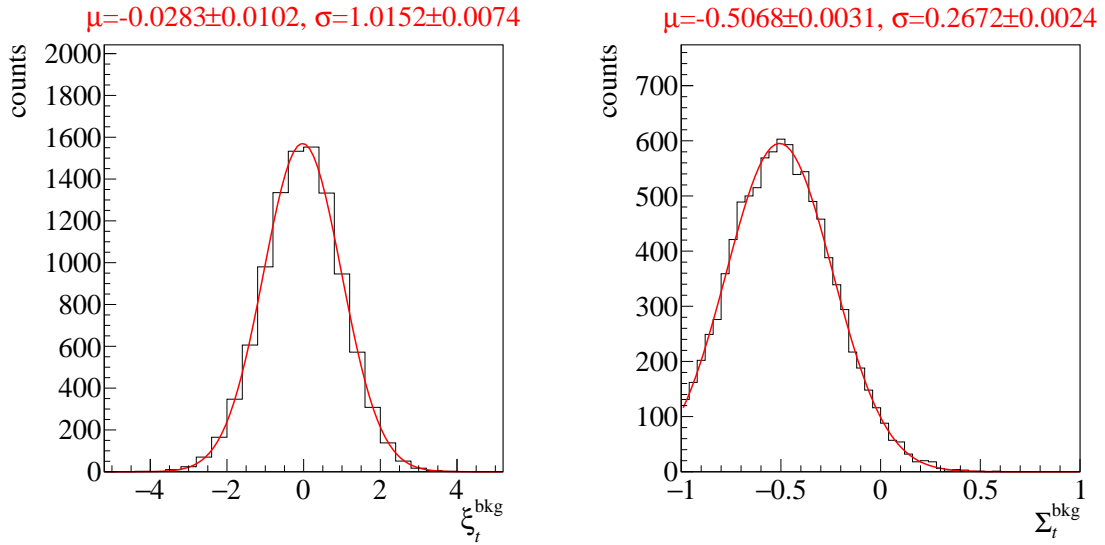


**Figure 4.17:** Normalized residuals (left) and unaltered distribution (right) of all 10000 fits for the background beam asymmetry  $\Sigma_t^{\text{bkg}}$ . GAUSSIAN fits are performed with results given on top of each plot.

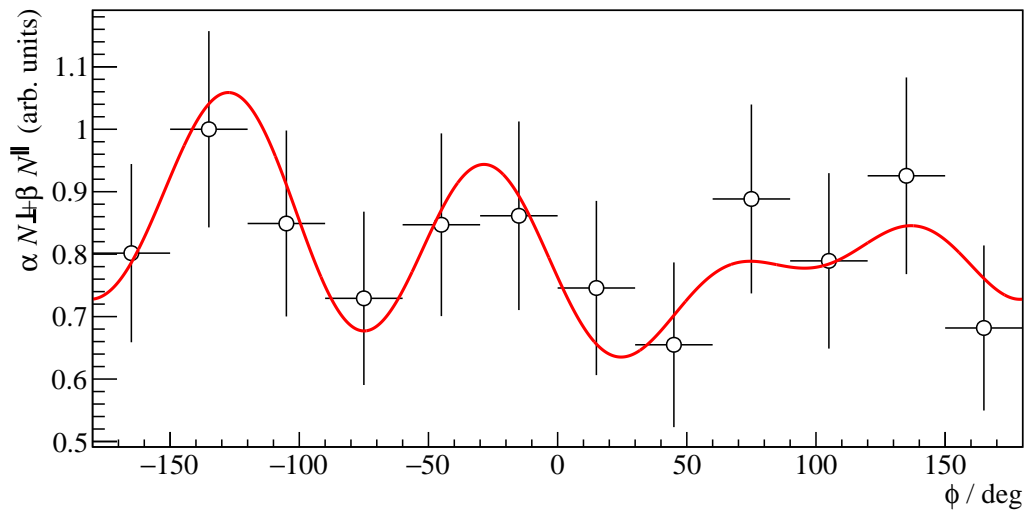


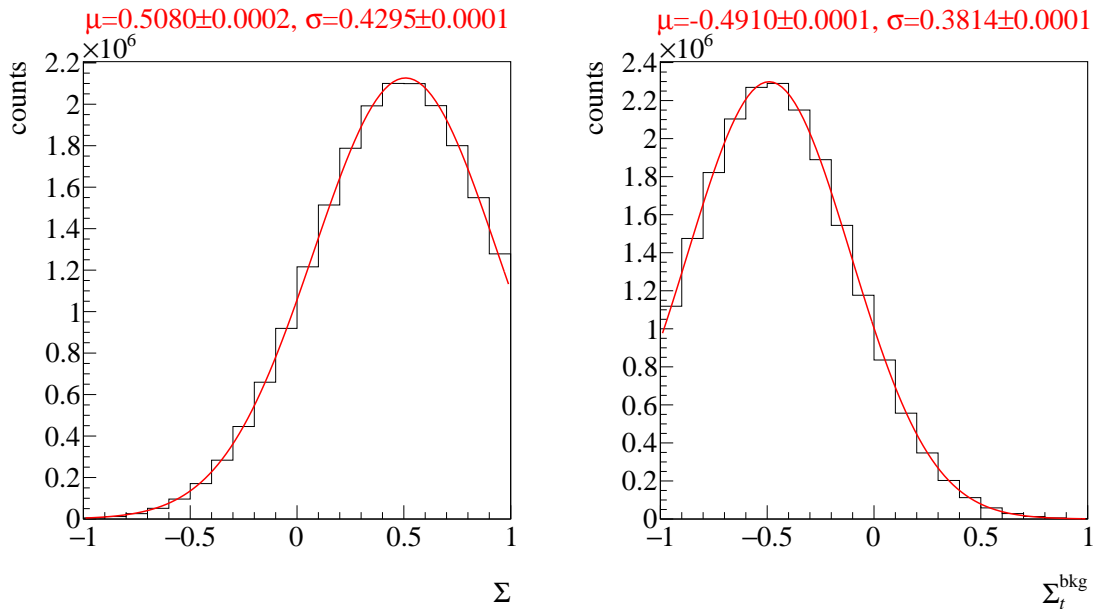
**Figure 4.18:** Fitted efficiency function (red line) applied to the polarization weighted sum of event yields (data points) for one toy Monte Carlo bin. 12 bins in  $\phi$  are built for demonstration.

With this  $\Sigma_2^{\text{true}}$  is added as an additional fit parameter to the probabilistic model, so that the likelihood is modified as

$$\begin{aligned} \ln \mathcal{L} = & \sum_{i=1}^n \ln p_{\text{prompt}} \left( \phi_i, p_{\gamma,i} \mid (1 - \delta) \cdot \Sigma_1 + \delta \cdot \Sigma_2^{\text{true}}, a, b, \Sigma_t^{\text{bkg}}, a^{\text{bkg}}, b^{\text{bkg}} \right) \\ & + \sum_{j=1}^m \ln p_{\text{sideband}} \left( \phi_j, p_{\gamma,j} \mid \Sigma_t^{\text{bkg}}, a^{\text{bkg}}, b^{\text{bkg}} \right). \end{aligned} \quad (4.45)$$

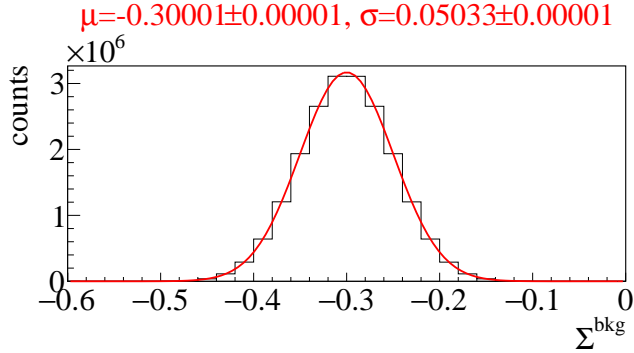
For a complete inference  $\Sigma_2^{\text{bkg}}$  also needs to be assigned a prior, which is chosen to be uniform to keep the number of fit parameters minimal. In total, 1000 bins in accordance with Table 4.2 are fitted with the adapted model that includes a background asymmetry  $\Sigma_2$  with statistical error  $\tau$  which are used to estimate the additional fit parameter  $\Sigma_2^{\text{true}}$ . For the sake of the toy Monte Carlo experiments the measurement error is arbitrarily chosen to be  $\tau = 0.05$ .

Figure 4.19 shows the combined posteriors for the fit parameters  $\Sigma_1$  and  $\Sigma_t^{\text{bkg}}$  of the event based BAYESIAN fit for all generated toy Monte Carlo bins. The posteriors are added up since the truncation of the posteriors biases the results when combining them in a pooled likelihood model or normalized residuals  $\Xi$ . Previous experiments already proved sensible error estimation, i.e. distribution widths, when using the unbinned BAYESIAN fit. This is discussed in appendix C. The input parameters are very well reproduced within the statistical error, which is given by the standard deviation of the GAUSSIAN. The posterior distribution of  $\Sigma_1$  is wider than the posterior of the background beam asymmetry  $\Sigma_t^{\text{bkg}}$  because an additional measurement of  $\Sigma_2$  with measurement error  $\tau$  is used to estimate  $\Sigma_1$ . This is in complete analogy to shifting the point estimates  $\Sigma^{\text{meas}}$  to their true values  $\Sigma^{\text{true}}$ , as described previously, which will also result in larger statistical error bars according to GAUSSIAN error propagation. Since



**Figure 4.19:** Combined (added) posteriors of all 1000 fits. Left: Signal beam asymmetry  $\Sigma_1$  Right: Background beam asymmetry  $\Sigma_t^{\text{bkg}}$ . A GAUSSIAN fit is performed with results given on top.

the signal beam asymmetry  $\Sigma_1$  was recognized correctly by the fit it is evident that the combined posterior distributions for  $\Sigma_2$  are in full agreement with the expectations, see figure 4.20. Mean  $\mu$  and standard deviation  $\sigma$  are reproduced exactly as they were modeled as a GAUSSIAN fit to the combined posteriors reveals.



**Figure 4.20:** Combined (added) posteriors of all fits for the fit parameter  $\Sigma_2^{\text{true}}$ . A GAUSSIAN fit is performed which reproduces exactly the values that were used for the simulations.

It remains to investigate the properties of the employed MARKOV chains. First of all one observes that the accuracy of results, i.e. the relative MCSE, suffers from the available statistics which are significantly smaller in comparison with the previously investigated case for the  $p\eta \rightarrow \gamma\gamma$  final state. Only 97% of all unbinned fits fulfill the self set criterion of  $\sigma_{\text{MCSE}}/\text{median}(p(\Sigma|y)) \leq 0.05$  whereas for the toy Monte Carlo experiments in the previous section 4.2 this was the case for *all* unbinned fits. This observation however is not resembling a failing fit but rather the possibility for the data to mimic beam asymmetries close to zero because of the fewer available data points. In these cases the relative MCSE exceeds the threshold as has also been observed before. Convergence and full exploration of the available parameter space on the other hand is guaranteed for all fits because all  $\hat{R}$  values for all parameters and fits are within the demanded thresholds.

Lastly, consistency of the fit results with the data that is fitted can be checked as before by a posterior predictive check of the detector coefficients  $a, b$  plugged into the efficiency function  $\epsilon(\phi) = \frac{1}{c} \cdot (\alpha \tilde{N}^\parallel + \beta \tilde{N}^\perp)$  as can be seen in Figure 4.22. Each draw  $a^{(s)}, b^{(s)}, s = 1, \dots, 20000$  is plotted as an opaque blue line. The mean over the posterior draws is indicated by the dashed line and follows the polarization weighted sum of event yields which is shown as data points. The mean agrees within statistical error bars at each point indicating finally a successful fit in every respect.

It has been demonstrated that the chosen BAYESIAN model can describe data generated with two beam asymmetries very well. Note that expanding the existing model from before requires minimal changes since *Stan* [**stan**] allows modular implementations; only the new parameter  $\Sigma_2^{\text{true}}$  and the new data points  $(\Sigma_2, \tau, \delta)$  have to be added to give correctly centered posteriors that are not anymore systematically shifted. More effort would have to be made to get similar results with the traditional unbinned fitting method described before.

### 4.3.2 Application of event based fit to data

Investigation of toy Monte Carlo experiments showed that the presence of polarized background events cause a systematic shift in the extracted beam asymmetry. The shift may be compensated by a modified

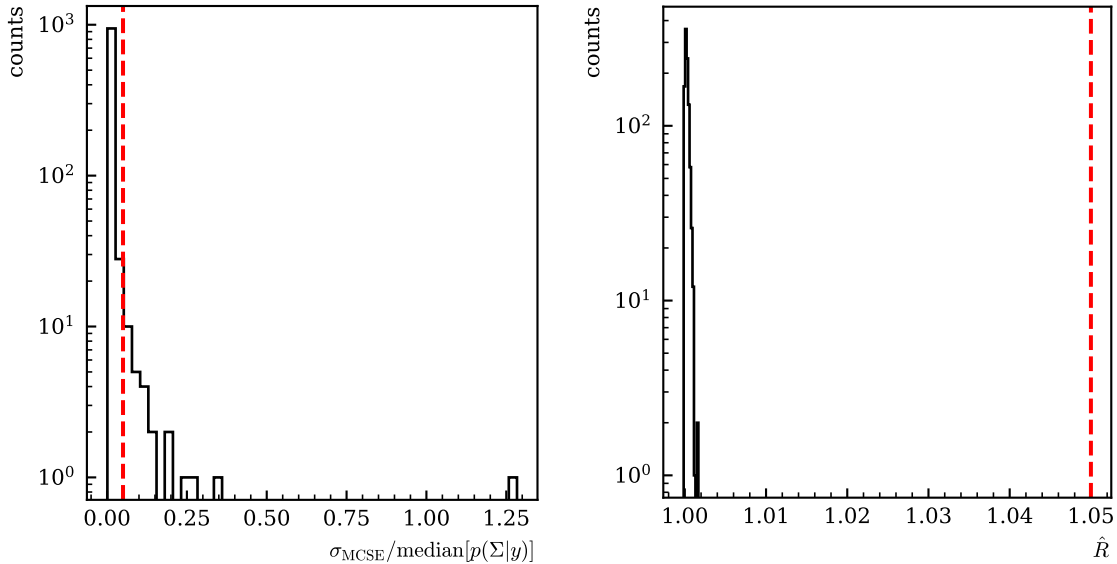


**Figure 4.21:** MCMC diagnostics for the event based BAYESIAN fit. Left: MCSE, Right:  $\hat{R}$ -value. The critical values not to be exceeded are marked by the dashed lines.

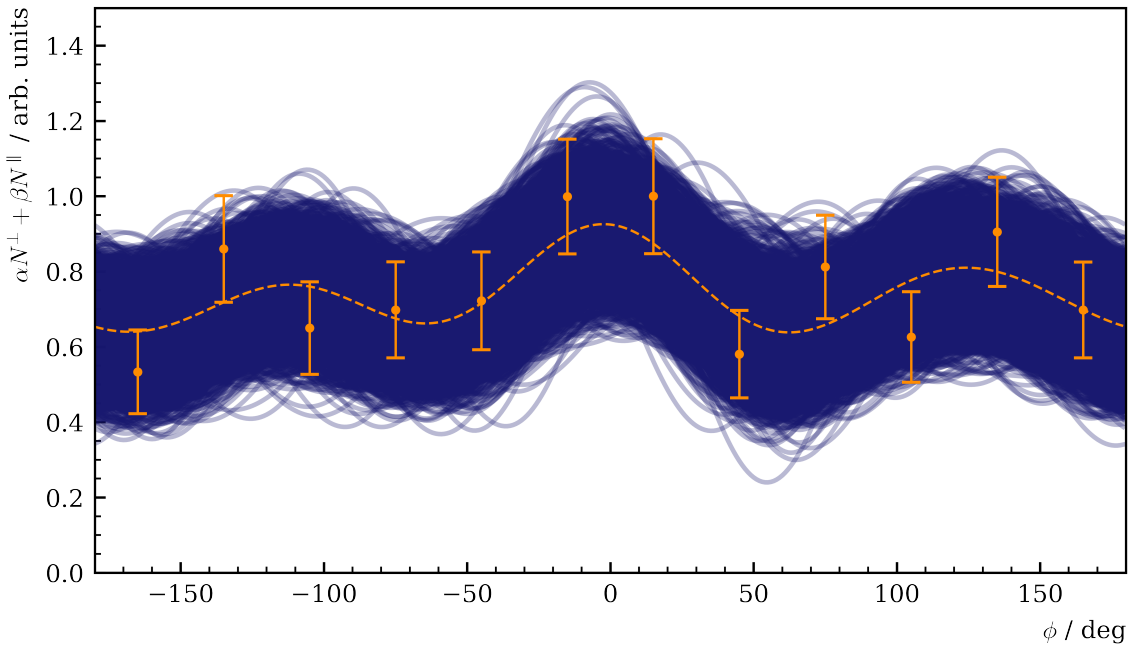


**Figure 4.22:** Posterior predictive checks of one toy Monte Carlo bin using the draws from the marginal posteriors of the detector coefficients  $a, b$  (opaque blue lines). The mean values are marked by the dashed line and follow the distribution of the data points which are the polarization weighted sum of event yields, using 12  $\phi$  bins.

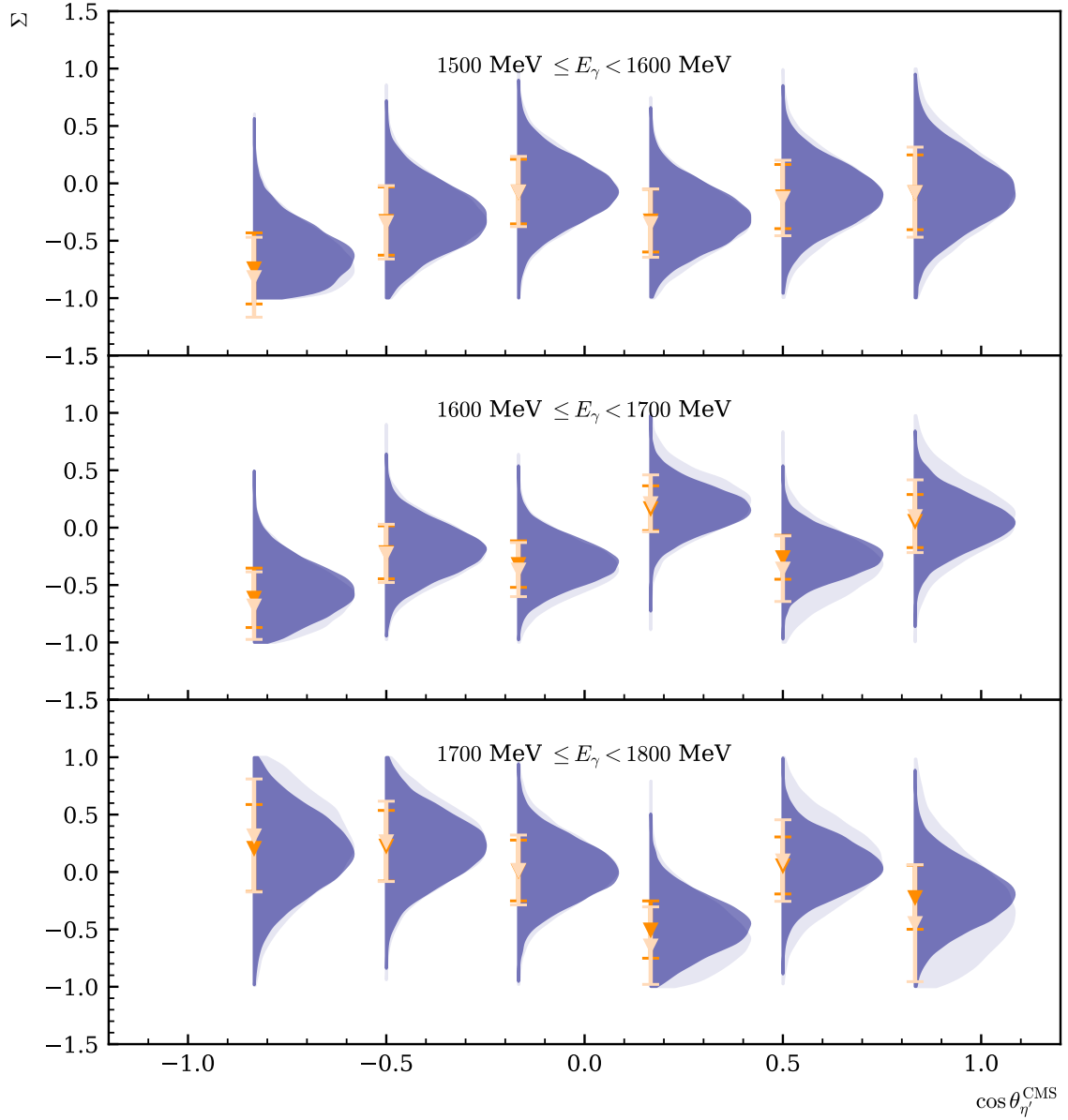
likelihood function for the BAYESIAN fit or by reversing the shift *after* obtaining intermediate results for  $\Sigma^{\text{meas}}$  with an unbinned maximum likelihood fit. By studying Monte Carlo simulations of various mesonic final states it has been found that the main background contributions in the analysis of the final state  $\gamma p \rightarrow p\eta' \rightarrow p\gamma\gamma$  is given by the false reconstruction of events  $\gamma p \rightarrow p2\pi^0 \rightarrow p4\gamma$ , see chapter 3. Conveniently, this includes the determination of the fraction of background events  $\delta$ , see Figure 3.10. Furthermore, preliminary results for the beam asymmetry in double pion photoproduction at the CBELSA/TAPS experiment using the same binning as this analysis [mahlbergphd] were available so that the previously discussed corrections can in fact be applied in each kinematic bin. It is hereby assumed that the *entire* background is realized by  $2\pi^0$  production and the fraction  $\delta$  is determined by an according fit of Monte Carlo spectra. This holds only approximately for each kinematic bin and is thus a source of systematic error, which is discussed in the next subsection 4.3.3.

Figure 4.23 shows the final results for the beam asymmetry in the reaction  $\gamma p \rightarrow p\eta' \rightarrow p\gamma\gamma$  obtained from data taken at the CBELSA/TAPS experiment. Shown are two sets of results; the dark blue distributions are the results of a unbinned BAYESIAN without any modifications to the original model whatsoever. The dark orange data points are the corresponding results of an unbinned maximum likelihood fit  $\Sigma^{\text{meas}}$ . The light blue distributions however depict the results that were obtained from the modified BAYESIAN model, i.e. with the additional fit parameter  $\Sigma_2^{\text{true}}$ , the light orange data points correspond to the corrected point estimates  $\Sigma^{\text{true}}$  according to Equation (4.42). In addition to the beam asymmetry  $\Sigma_1 = \Sigma_{\eta'}$  the fit also determines marginal posteriors for  $\Sigma_2^{\text{true}} = \Sigma_{2\pi^0}$ . To check consistency of the fit, these posterior distributions are compared to the results  $(\Sigma_2, \tau)$  that were used as input [mahlbergphd], they are shown in Figure 4.24.

Several remarks can be made regarding these results:

1. As has been found studying toy Monte Carlo simulations, the modified BAYESIAN fit again successfully reconstructs two separate beam asymmetries. Figure 4.24 impressively shows the good agreement of input data points  $(\Sigma_2, \tau)$  and posterior of  $\Sigma_2^{\text{true}}$ . On average  $\Sigma_2 \pm \tau$  covers 68% of the posterior distributions, corresponding to a  $1\sigma$  region, proving that no systematic error is made by introducing the additional fit parameter  $\Sigma_2^{\text{true}}$ .
2. There is very good agreement between point estimates and corresponding posterior distributions. The point estimates give mean and standard deviation of the marginal posteriors to good approximation. If the point estimates are corrected according to Equation (4.42) their statistical error increases. Similarly, the distributions from the modified BAYESIAN fit are wider, agreeing with the corrected point estimates and errors.
3. Errors and distributions widths are rather large, which could be expected due to the small amount of events that could be used to extract the results. However, distributions are rarely truncated because they are mostly centered around  $\Sigma \approx 0$
4. Shifting the final results of the beam asymmetry depending on the amount of background has marginal impact on the absolute scale. Although background contributions are far from negligible they exhibit only asymmetries close to 0 (see Figure 4.24). Thus, the shifted values still agree within statistical error bars or widths with the original values.

To confirm between- and in-chain convergence for all fits, the  $\widehat{R}$ -values of all fit parameters are checked to be  $1 \lesssim \widehat{R} < 1.05$ . Due to the large number of samples this criterion is fulfilled without complications. Furthermore the relative MCSE with respect to the median of the posterior distributions



**Figure 4.23:** Final results for the beam asymmetry  $\Sigma$  in  $\eta'$  photoproduction. Two sets of results are shown: The dark blue distributions and orange data points with errorbars are obtained with an unbinned fit that does not consider any background contributions. The light blue distributions and data points are obtained with the modified BAYESIAN fit and by correcting the point estimates according to Equation (4.42), respectively. All errors are statistical errors only.

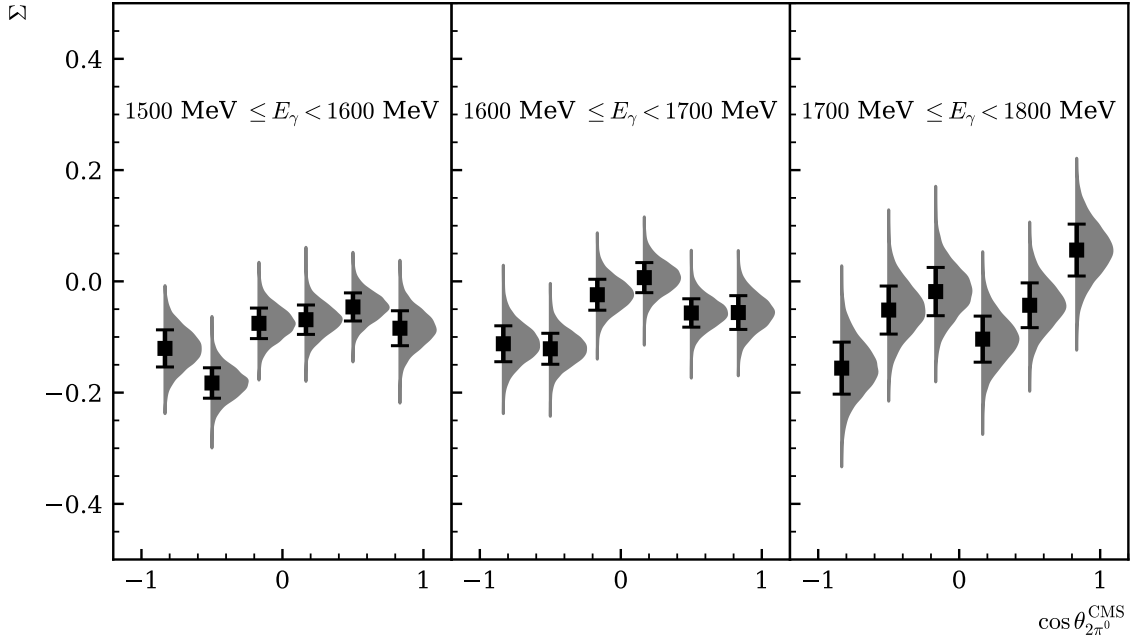


**Figure 4.24:** Results for the additionally fitted  $\Sigma_2^{\text{true}}$  (distributions) compared with the underlying data points [mahlbergphd] with statistical errors. The error bars on average cover  $1\sigma$  of the distributions, indicating a successful fit. All errors are statistical errors only.

is checked to confirm the accuracy of all chains. It is  $\sigma_{\text{mcse}}/\text{median } (p(\Sigma|y)) \leq 0.05$  for all but one fit where the beam asymmetry is very close to zero. Figure 4.25 shows both quantities for all fits.

A last consistency check of the posterior predictive distributions of the efficiency function reveals no results aside from the expectations. Figure 4.26 shows all posterior predictive draws of the detector coefficients  $a^{(s)}, b^{(s)}$  plugged into the efficiency function  $\epsilon(\phi)$ . The mean of all draws describes the polarization weighted sum of event yields within statistical errors. The observed efficiency is less peaked than the simulated one (Figure 4.22), confirming the results that have been found in section 4.2. Yet, more inefficiencies are observed compared to the  $p\eta$  final state due to the decreased statistics.

### 4.3.3 Systematic error

There are two major sources for systematic error in the discussed analysis. On one hand, the determination of the polarization degree of the incident photon beam is not exactly accurate and thus influences the fit results which heavily depend on the linear polarization degree. On the other hand, neglecting polarized background events that have been falsely regarded as  $2\pi^0$  events when shifting the intermediate results may create systematic errors.

The relative error of the polarization degree can be estimated during the determination process where analytically calculated bremsstrahlung spectra (ANB) are fitted to measured spectra [Afz19].

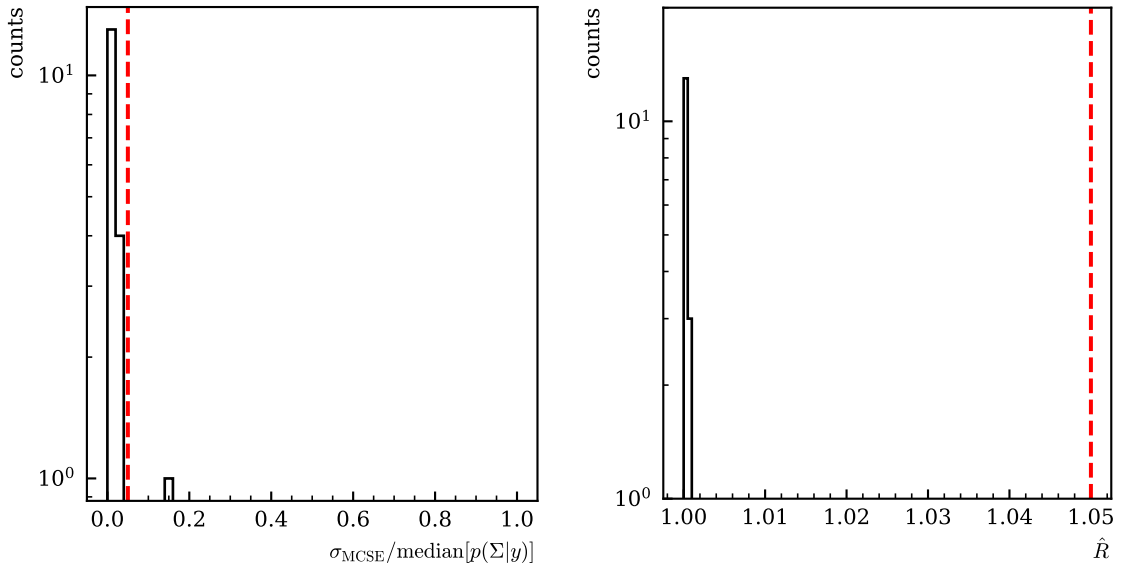


**Figure 4.25:** MCMC diagnostics for the event based BAYESIAN fit. Left: MCSE, Right:  $\hat{R}$ -value. The critical values not to be exceeded are marked by the dashed lines.

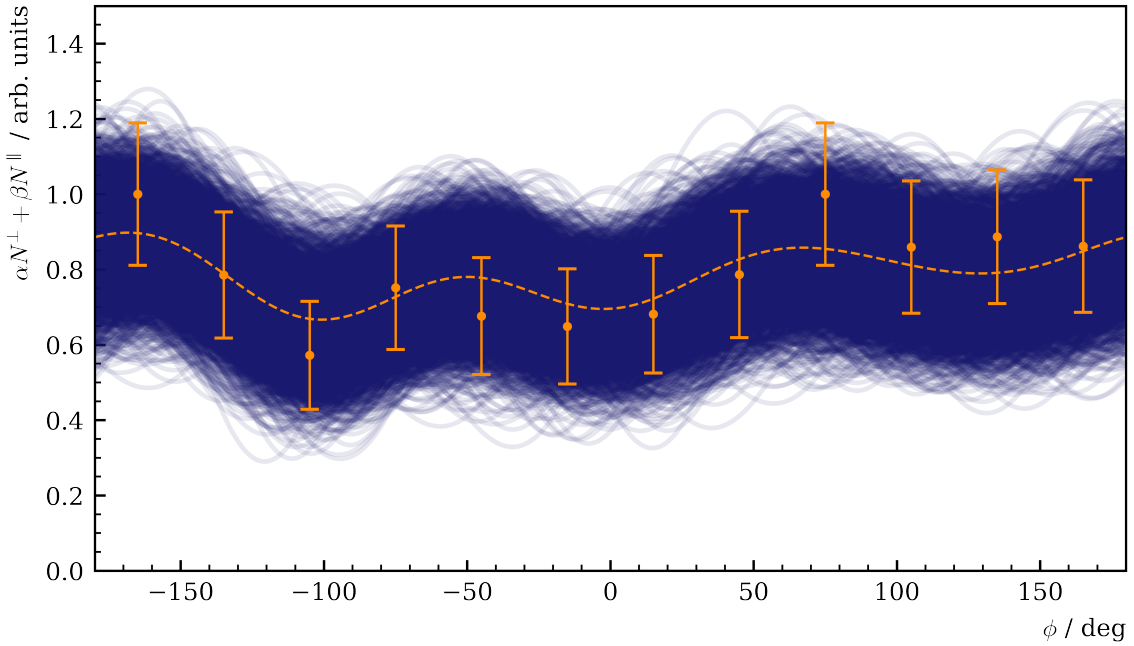


**Figure 4.26:** Posterior predictive checks of the kinematic bin  $1700 \text{ MeV} \leq E_\gamma < 1800 \text{ MeV}, 0.67 \leq \cos \theta < 1$  using the draws from the marginal posteriors of the detector coefficients  $a, b$  (opaque blue lines). The mean values are marked by the dashed line and follow the distribution of the data points which are the polarization weighted sum of event yields, using 12  $\phi$  bins.

This allows to give the relative error in the beam energy region that was analyzed as [Afz19]

$$\frac{\Delta p_\gamma}{p_\gamma} = \begin{cases} 0.05, & \text{if } E_\gamma < 1600 \text{ MeV} \\ 0.08, & \text{otherwise.} \end{cases} \quad (4.46)$$

It was assumed that

$$\Sigma^{\text{meas}} = (1 - \delta) \cdot \Sigma^{\text{true}} + \delta \Sigma^{\text{bkg}}, \quad (4.47)$$

with  $\Sigma^{\text{true}} = \Sigma_{\eta'}$  and  $\Sigma^{\text{bkg}} = \Sigma_{2\pi^0}$  and according modifications to the obtained results have been made. However regarding the entire background contributions to double pion photoproduction holds only approximately in each bin. Actually, the measured value for the beam asymmetry is given by

$$\Sigma^{\text{meas}} = (1 - \delta_1 - \delta_2) \cdot \Sigma_{\eta'} + \delta_1 \Sigma_{2\pi^0} + \delta_2 \Sigma^{\text{bkg}}, \quad (4.48)$$

where  $\delta_1$  is the relative contribution of  $2\pi^0$  production events and  $\delta_2$  the relative contribution of other background events, e.g.  $\pi^0\eta$  production, that have been neglected before that may exhibit an asymmetry  $\Sigma^{\text{bkg}}$ . The systematic uncertainty of  $\Sigma_{\eta'}$  can then be determined by setting  $\Sigma^{\text{bkg}} = \pm 1$  and determining the maximum deviation from the previous results. The results from the unbinned maximum likelihood fit are used which to good approximation also give the median and mean of the posterior distributions.

$$\Delta \Sigma_{\eta'} = \max \left[ \left| \frac{\Sigma^{\text{meas}} - \delta_1 \cdot \Sigma_{2\pi^0} \pm \delta_2 \cdot 1}{1 - \delta_1 - \delta_2} - \frac{\Sigma^{\text{meas}} - \delta \cdot \Sigma_{2\pi^0}}{1 - \delta} \right| \right] \quad (4.49)$$

The total absolute systematic error is then given by

$$\Delta \Sigma_{\eta'}^{\text{sys}} = \sqrt{\left( \frac{\Delta p_\gamma}{p_\gamma} \Sigma_{\eta'} \right)^2 + (\Delta \Sigma_{\eta'})^2}. \quad (4.50)$$

Figure 4.27 shows all results with systematic uncertainties given on the bottom of each plot.

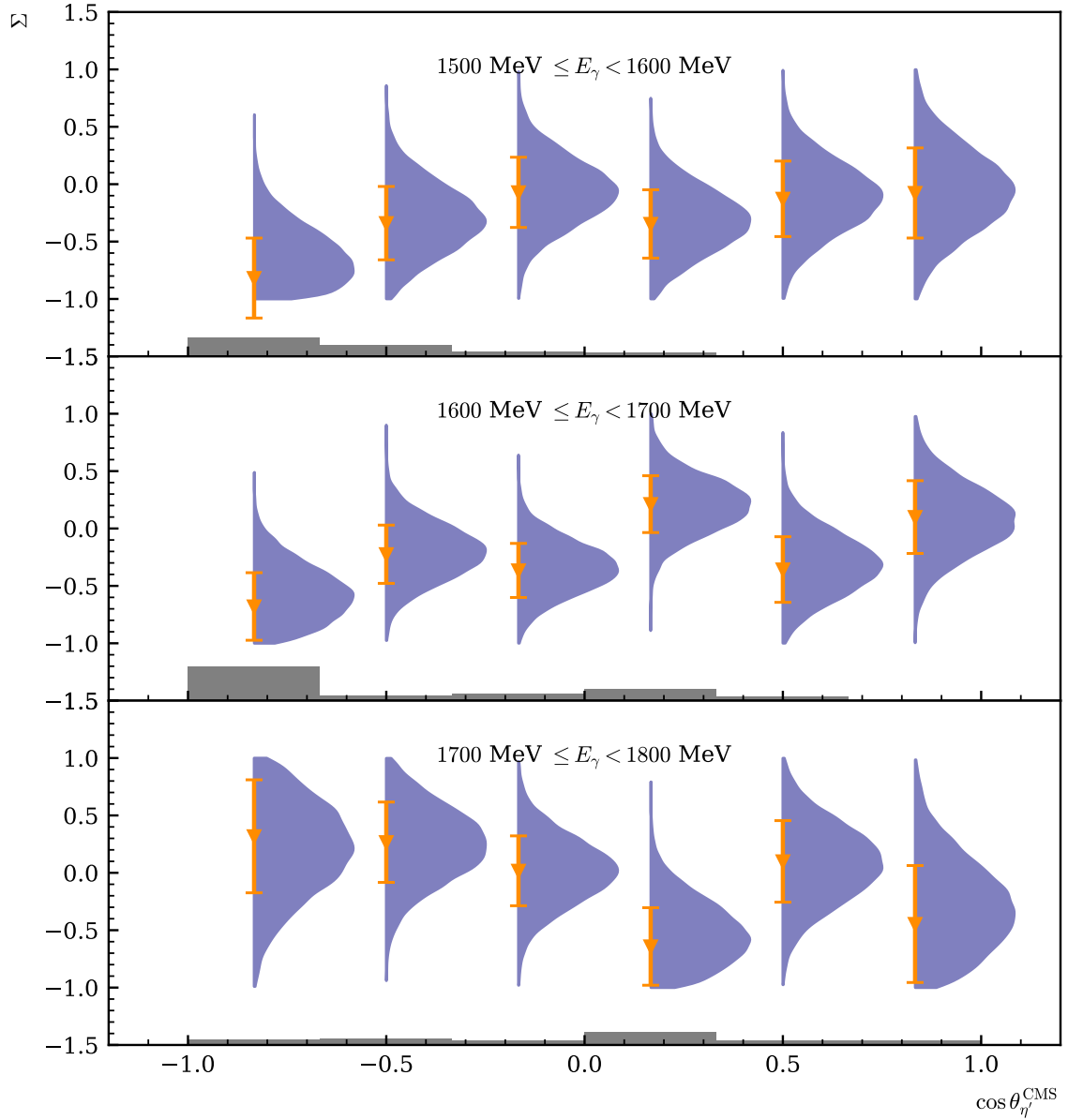


**Figure 4.27:** Final results for the beam asymmetry  $\Sigma_{\eta'}$  for all energy and angular bins. Only the corrected results from the unbinned maximum likelihood fit and distributions from the modified BAYESIAN fit are shown. The bottom of each plot indicates the systematic error as gray bars. It was determined as previously discussed.



# APPENDIX A

---

## Additional plots and calculations

---

This chapter will give additional calculations and plots which would have interrupted the train of thought unnecessarily in the main part.

### A.1 Statistical error for the asymmetry $A(\phi)$

Let  $\tilde{N}_i^{\parallel/\perp}$  be the normalized event yields at bin  $\phi_i$ . As mentioned in section 4.1, the asymmetry  $A_i$  at bin  $i$  is then given by

$$A_i = \frac{\tilde{N}_i^\perp - \tilde{N}_i^\parallel}{p_\gamma^\parallel \tilde{N}_i^\perp + p_\gamma^\perp \tilde{N}_i^\parallel} = \Sigma \cos(2(\alpha^\parallel - \phi_i)), \quad (\text{A.1})$$

where the event yields are normalized over all  $M$   $\phi$ -bins

$$\tilde{N}_i^{\parallel/\perp} = \frac{N_i^{\parallel/\perp}}{\sum_{j=1}^M N_j^{\parallel/\perp}}.$$

To estimate statistical errors according to GAUSSIAN error propagation, the partial derivatives with respect to  $\tilde{N}_i^{\parallel/\perp}$  have to be built:

$$(\Delta A_i)^2 = \left( \frac{\partial A_i}{\partial \tilde{N}_i^\parallel} \Delta \tilde{N}_i^\parallel \right)^2 + \left( \frac{\partial A_i}{\partial \tilde{N}_i^\perp} \Delta \tilde{N}_i^\perp \right)^2, \quad (\text{A.2})$$

where

$$\left( \frac{\partial A_i}{\partial \tilde{N}_i^{\parallel/\perp}} \right)^2 = \left[ \frac{\tilde{N}_i^{\perp/\parallel} (p_\gamma^\perp + p_\gamma^\parallel)}{(p_\gamma^\parallel \tilde{N}_i^\perp + p_\gamma^\perp \tilde{N}_i^\parallel)^2} \right]^2, \quad (\text{A.3})$$

$$\text{and with } \tilde{N}_i^{\perp/\parallel} = \tilde{N}_i \quad (\text{A.4})$$

$$(\Delta \tilde{N}_i)^2 = \left[ \frac{\partial}{\partial N_i} \left( \frac{N_i}{\sum_j N_j} \right) \cdot \Delta N_i \right]^2 + \sum_{j \neq i} \left[ \frac{\partial}{\partial N_j} \left( \frac{N_i}{\sum_j N_j} \right) \cdot \Delta N_j \right]^2 \quad (\text{A.5})$$

$$= \left[ \frac{\sum_{j \neq i} N_j}{\left( \sum_j N_j \right)^2} \cdot \Delta N_i \right]^2 + \sum_{j \neq i} \left[ -1 \cdot \frac{N_i}{\left( \sum_j N_j \right)^2} \cdot \Delta N_j \right]^2 \quad (\text{A.6})$$

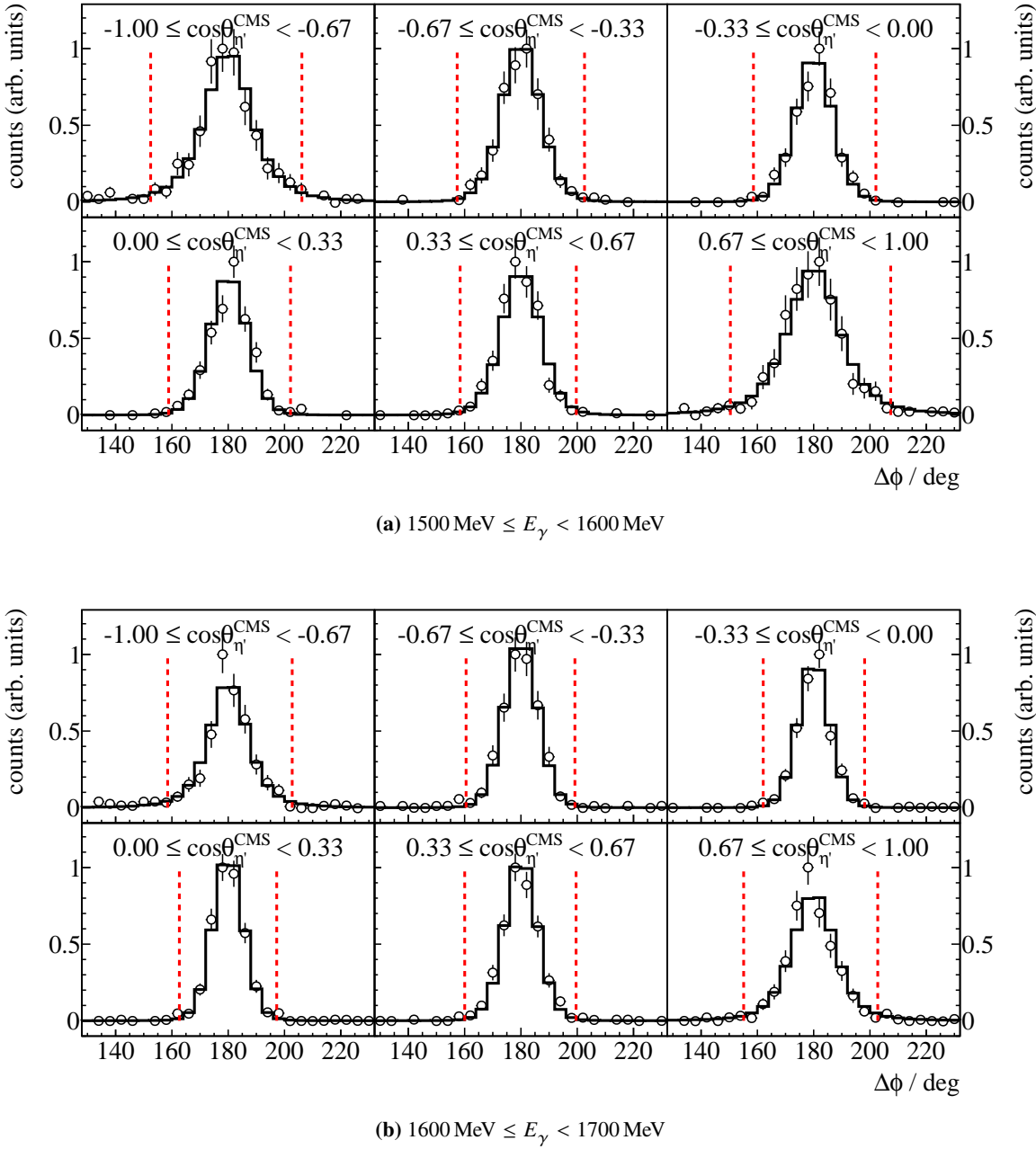
$$= \frac{1}{\left( \sum_j N_j \right)^4} \cdot \left[ \left( \sum_{j \neq i} N_j \cdot \Delta N_i \right)^2 + \sum_{j \neq i} \left( N_i \cdot \Delta N_j \right)^2 \right]. \quad (\text{A.7})$$

One can then further use that  $(\Delta N_i)^2 \approx N_i$ . This holds only approximately, since the histograms are filled  $N$  times with weights  $w_n$  (see chapter 3.3), but since the weights are either  $w = 1$  or  $w \ll 1$

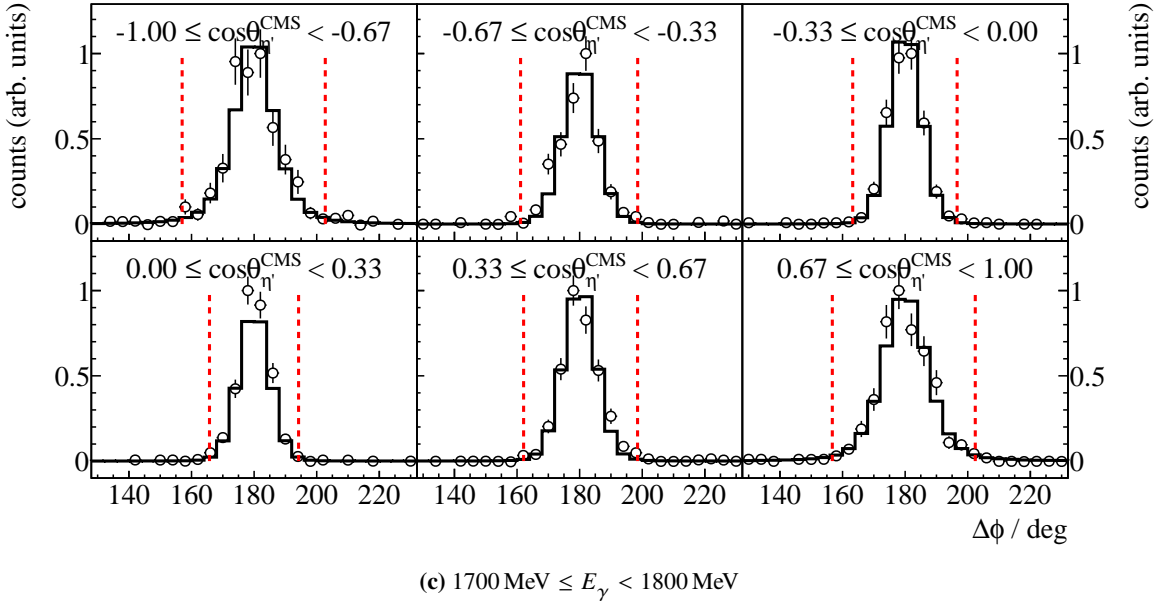
$$\Delta N_i = \sqrt{\sum_{n=1}^N w^2} \approx \sqrt{N_i}. \quad (\text{A.8})$$

## A.2 Kinematic variables for each bin

### A.2.1 Coplanarity



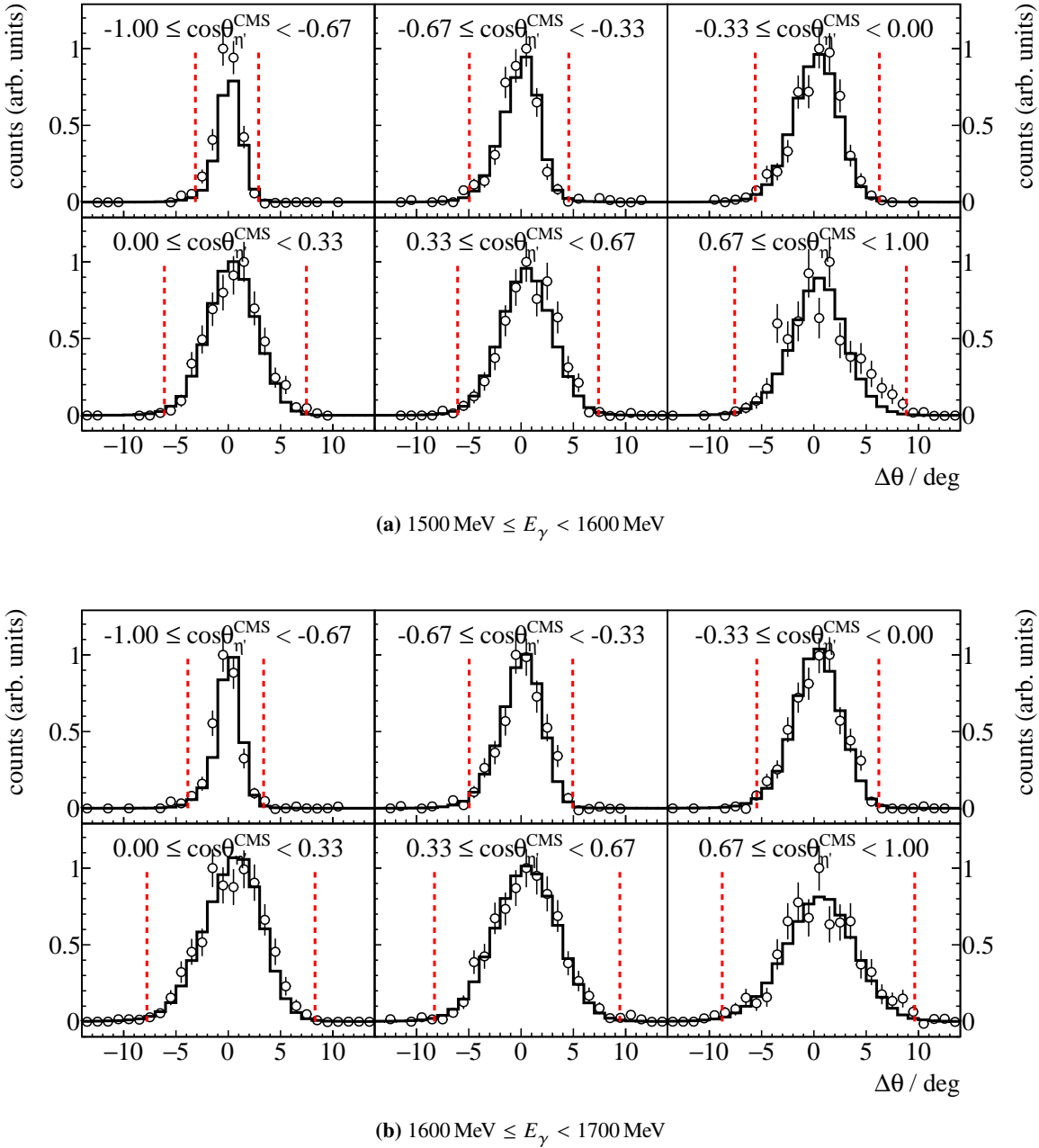
**Figure A.1:** Coplanarity  $\Delta\phi$  for all energy and angular bins. Data points are displayed as open circles, scaled Monte Carlo data belonging to  $\eta'$  photoproduction is displayed as solid histogram. The determined cut ranges are indicated by the dashed red lines.



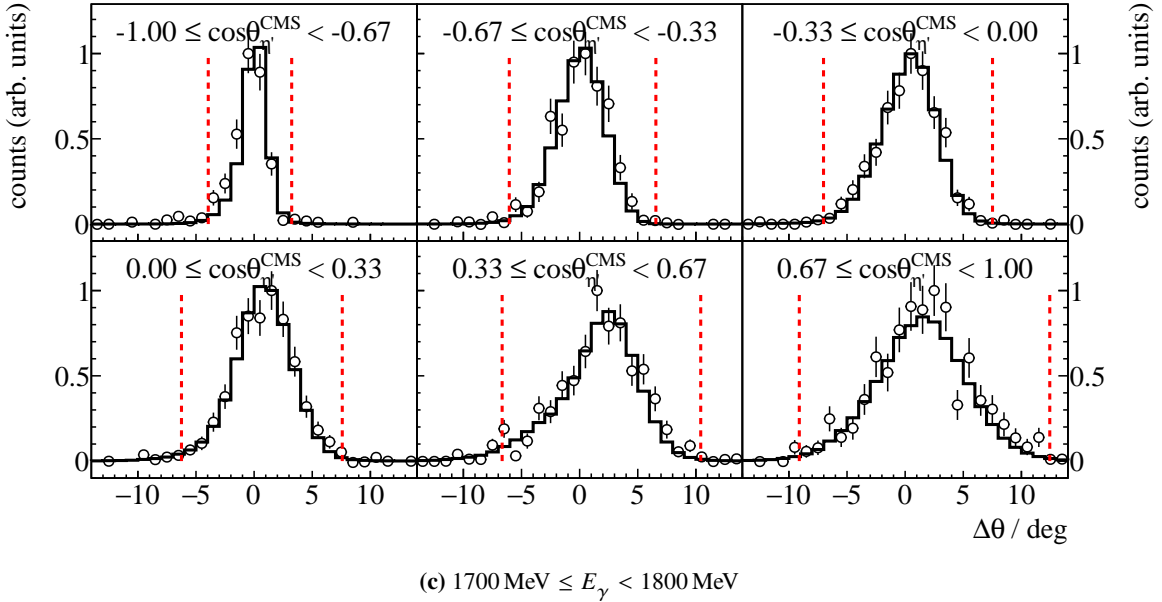
**Figure A.1:** Coplanarity  $\Delta\phi$  for all energy and angular bins. Data points are displayed as open circles, scaled Monte Carlo data belonging to  $\eta'$  photoproduction is displayed as solid histogram. The determined cut ranges are indicated by the dashed red lines.

Figure A.1 shows the coplanarity for all energy and angular bins. Cut ranges were determined from a GAUSSIAN fit to the data points. Only slight dependency on beam energy and meson polar angle can be identified. Only  $\eta'$  Monte Carlo data are fitted because the measured points do not give enough reference points for the fit to identify different contributing final states. There is good agreement between Monte Carlo simulations and measured data.

### A.2.2 Polar angle difference



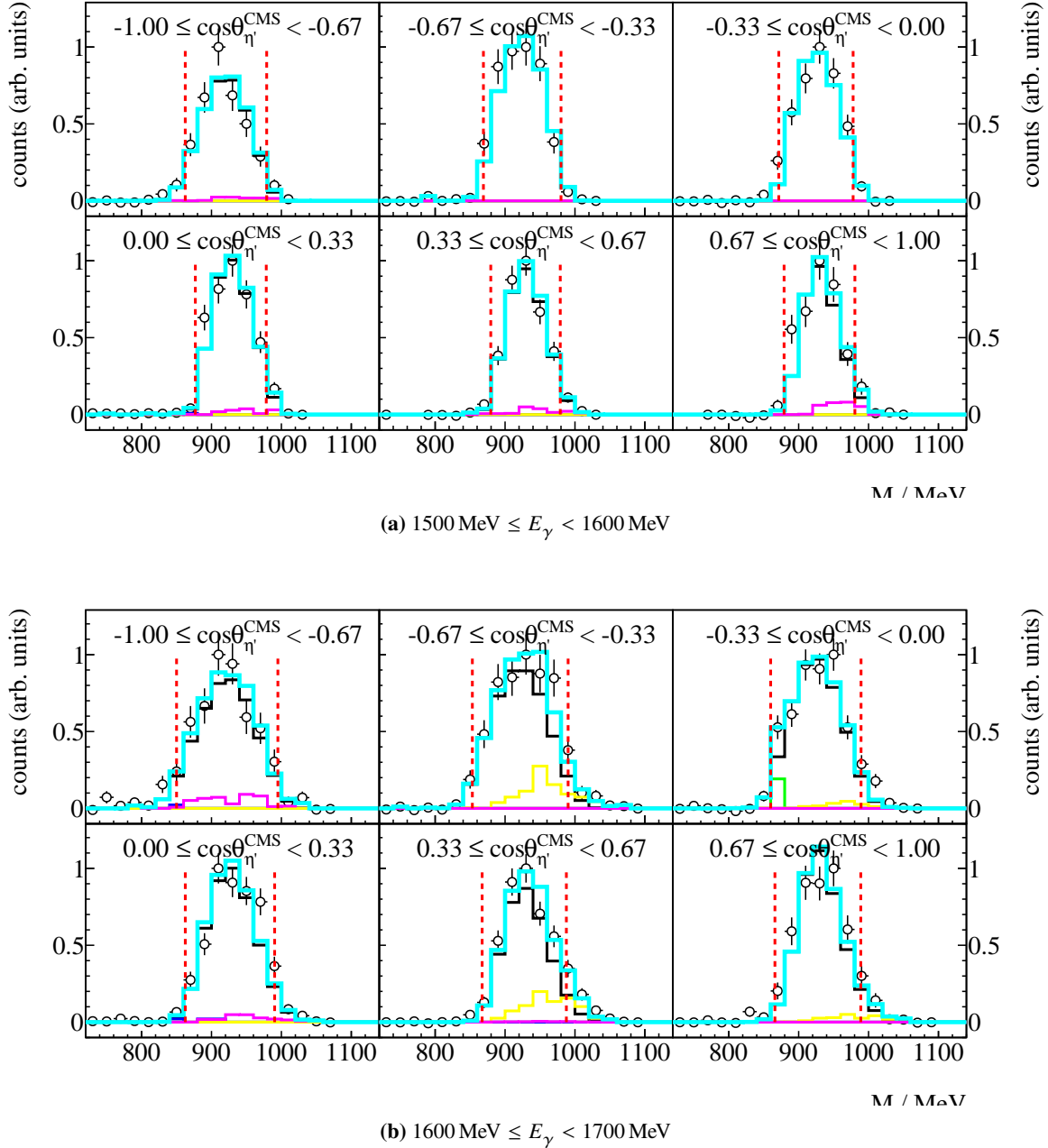
**Figure A.2:** Polar angle difference  $\Delta\theta$  for all energy and angular bins. Data points are displayed as open circles, scaled Monte Carlo data belonging to  $\eta'$  photoproduction is displayed as solid histogram. The determined cut ranges are indicated by the dashed red lines.



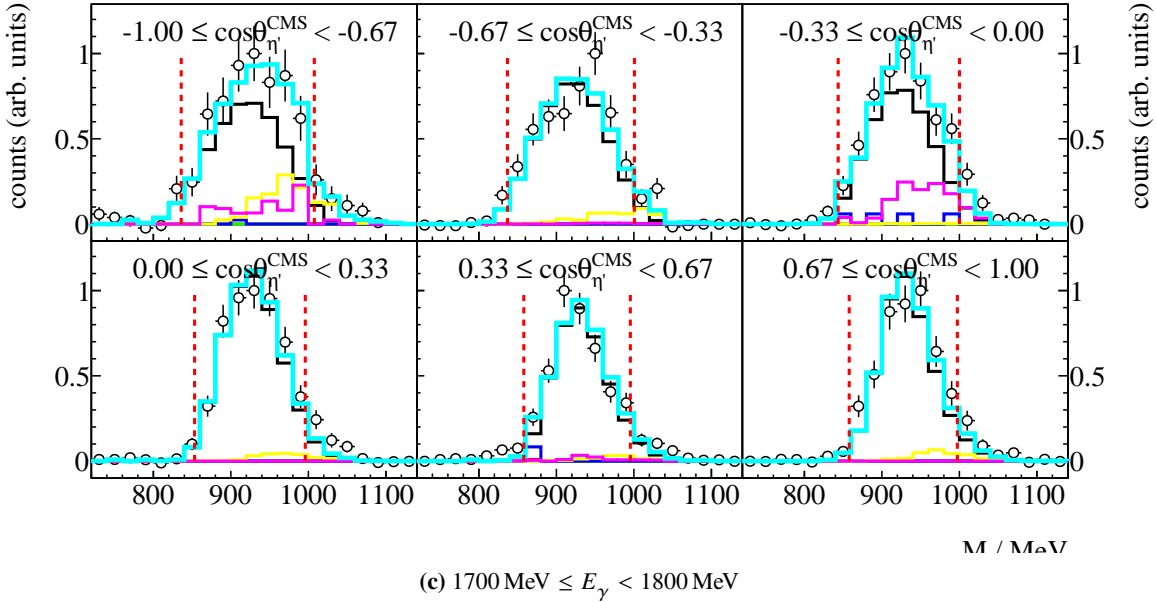
**Figure A.2:** Polar angle difference  $\Delta\theta$  for all energy and angular bins. Data points are displayed as open circles, scaled Monte Carlo data belonging to  $\eta'$  photoproduction is displayed as solid histogram. The determined cut ranges are indicated by the dashed red lines.

Figure A.2 shows the polar angle difference for all energy and angular bins. Cut ranges were determined from a GAUSSIAN fit to the data points. Only slight dependency on beam energy can be identified whereas clear correlation between width of the distribution and meson polar angle exists. This is due to the hit detectors which exhibit different angular resolutions, as has been discussed in the main part. Only  $\eta'$  Monte Carlo data are fitted because the measured points do not give enough reference points for the fit to identify different contributing final states. There is good agreement between Monte Carlo simulations and measured data.

### A.2.3 Missing mass



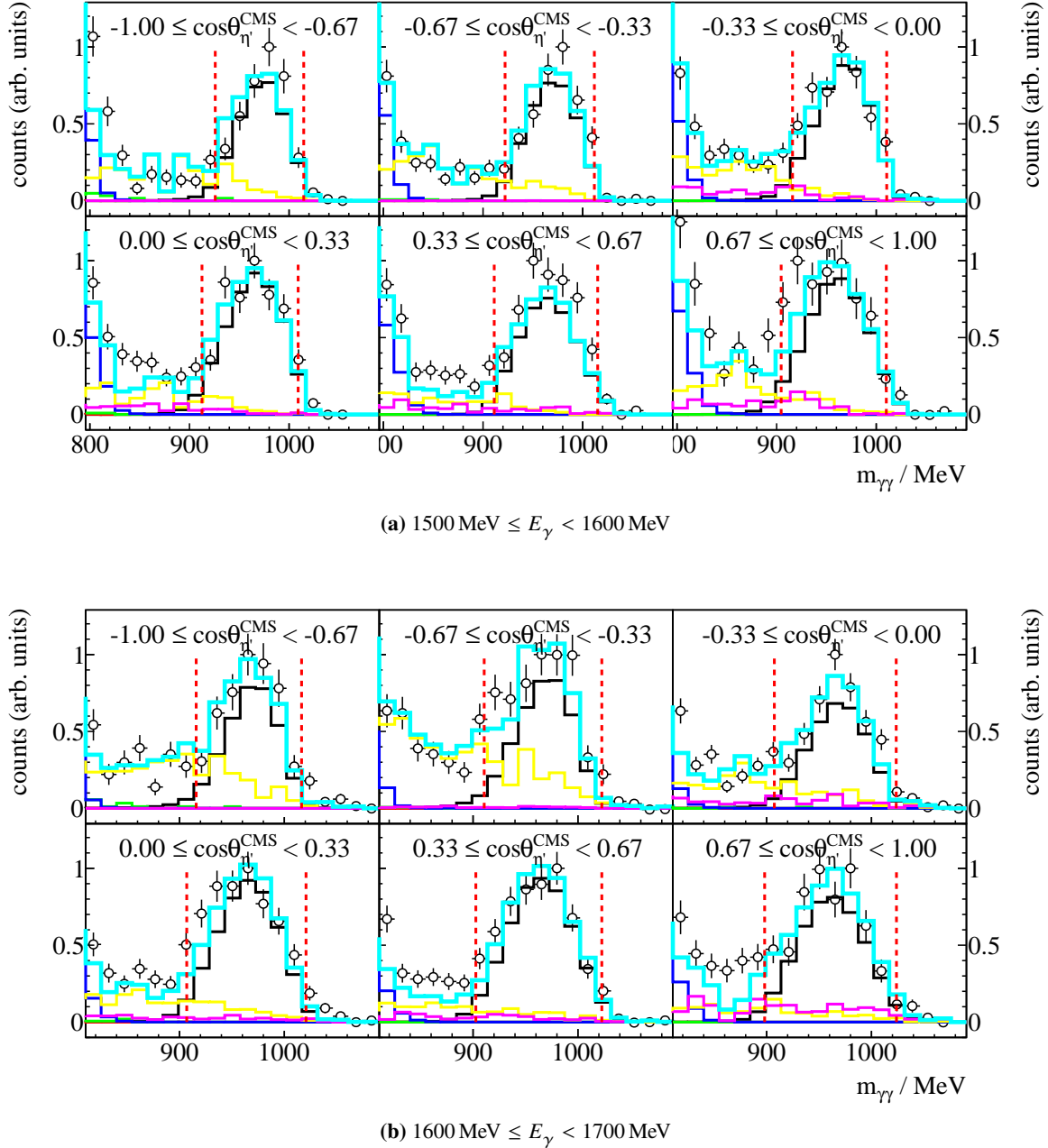
**Figure A.3:** Missing mass  $m_x$  for all energy and angular bins. Data points are displayed as open circles, scaled Monte Carlo data belonging to  $\eta'$  (black),  $2\pi^0$  (yellow) and  $\pi^0\eta$  (magenta) photoproduction is displayed as solid histogram while their sum is displayed as turquoise histogram. The determined cut ranges are indicated by the dashed red lines.



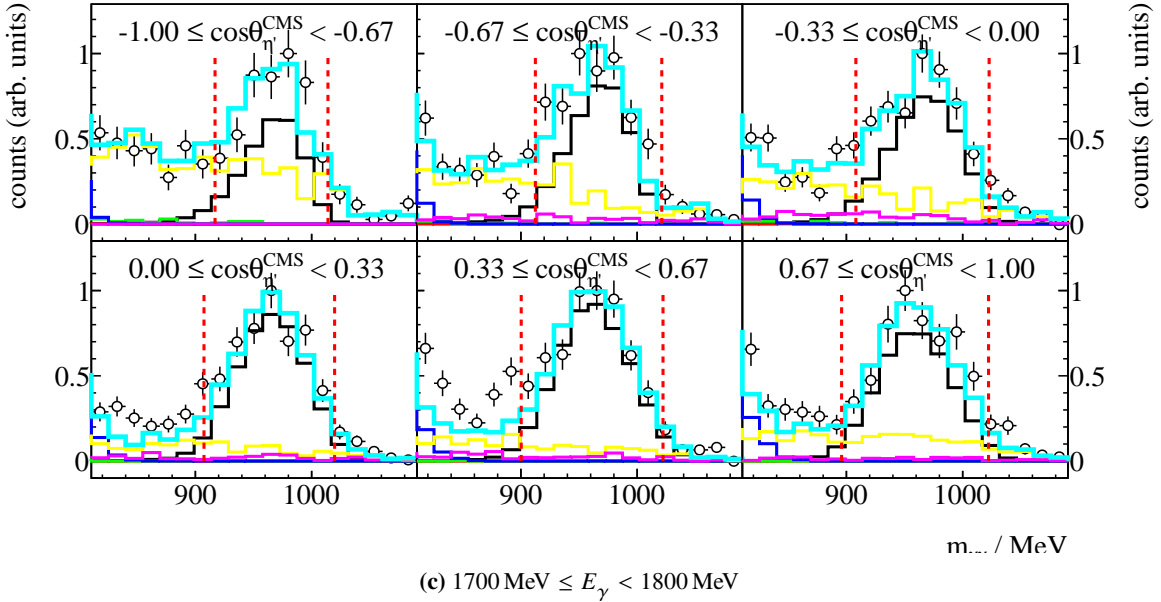
**Figure A.3:** Missing mass  $m_X$  for all energy and angular bins. Data points are displayed as open circles, scaled Monte Carlo data belonging to  $\eta'$  (black),  $2\pi^0$  (yellow) and  $\pi^0\eta$  (magenta) photoproduction is displayed as solid histogram while their sum is displayed as turquoise histogram. The determined cut ranges are indicated by the dashed red lines.

Figure A.3 shows the missing mass for all energy and angular bins. Cut ranges were determined from a Novosibirsk fit to the Monte Carlo data. Only slight dependency on meson polar angle can be identified. Especially at higher beam energies the missing mass peak grows wider with flat background contributions from  $2\pi^0$  and  $\pi^0\eta$  production towards higher masses. The Monte Carlo fit mostly shows consistency with the fit of the invariant mass spectra. However, spectra are to be seen with caution, since the shapes of the two different background contributions are very similar and there is no other reference point in the missing mass spectrum as opposed to the invariant mass. Fits to the invariant mass spectra may reveal background contributions where a fit to the missing mass spectrum failed to find any. There is good agreement between Monte Carlo simulations and measured data.

### A.2.4 Invariant mass



**Figure A.4:** Invariant mass  $m_{\text{meson}}$  for all energy and angular bins. Data points are displayed as open circles, scaled Monte Carlo data belonging to  $\eta'$  (black),  $2\pi^0$  (yellow),  $\pi^0\eta$  (magenta),  $\pi^0$  (green) and  $\omega$  (blue) photoproduction is displayed as solid histogram while their sum is displayed as turquoise histogram. The determined cut ranges are indicated by the dashed red lines.



**Figure A.4:** Invariant mass  $m_{\text{meson}}$  for all energy and angular bins. Data points are displayed as open circles, scaled Monte Carlo data belonging to  $\eta'$  (black),  $2\pi^0$  (yellow),  $\pi^0\eta$  (magenta),  $\pi^0$  (green) and  $\omega$  (blue) photoproduction is displayed as solid histogram while their sum is displayed as turquoise histogram. The determined cut ranges are indicated by the dashed red lines.

Figure A.4 shows the invariant mass for all kinematic bins. Hardly any dependence on meson direction and beam energy is observed. However, background contributions are especially observed in very forward and backward direction towards higher beam energies in consistency with findings from the missing mass spectra. A flat background is realized by  $2\pi^0$  and  $\pi^0\eta$  production. There is good agreement between Monte Carlo simulations and measured data.

## APPENDIX B

---

### Discussion of binned fits

---

Investigation of toy Monte Carlo experiments (cf. section 4.3) revealed that the choice of binning leads to systematic errors regarding the parameter  $\Sigma$  when fitting a binned distribution to the equation

$$A(\phi) = \Sigma \cdot \cos(2(\alpha^{\parallel} - \phi)). \quad (\text{B.1})$$

To investigate this further, the distributions  $A(\phi)$  from different toy Monte Carlo experiments where fitted for several binnings in  $\phi$ . Three different Monte Carlo experiments were considered, each corresponding roughly to the expected statistics in one kinematic bin for  $\pi^0$ ,  $\eta$  and  $\eta'$  photoproduction, respectively. For simplicity's sake, only least squares fits are shown here, although similar results were found for BAYESIAN fits also. The equivalency of BAYESIAN and least squares fit has been demonstrated sufficiently up until now. To identify the bias that is introduced by binning the data, 10000 toy Monte Carlo bins for each setting are fitted for  $n = 10, 15, 20, \dots, 100$  bins. Then the dependence from the amount of bins of the mean  $\mu$  of the normalized residuals  $\xi$  as well as the mean  $\chi^2$  value of all fits is investigated. This is shown in Figure B.1; The fitted mean of the normalized posteriors  $\xi$  is plotted against the number of bins (blue data points, left ordinate) as well as the mean  $\chi^2$  of 10000 fits depending on the number of bins (red data points, right ordinate). Clear dependencies can be made out: while too few bins tend to underestimate the true value of the beam asymmetry, too much bins will lead to an overcompensation. For this reason, the functions  $\chi^2(n)$  and  $\mu(n)$  are monotonously rising with increasing number of bins  $n$ . An exception is realized by the samples that simulated the statistics of the  $\eta'$  final state, which can be explained by the fact, that after reaching a certain number of bins, no sensible fit estimates can be made anymore because too few data points are available. A minimum deviation from the nominal value is reached with  $n = 10, 20, 30$  bins for statistics comparable to  $\eta'$ ,  $\eta$  and  $\pi^0$  production respectively. This does not coincide with a minimum  $\chi^2$  necessarily, although the mean  $\chi^2$  values associated with the best estimation of the input value are compatible with 1. Figure B.1 however remarkably shows the influence binning has on the extraction of the beam asymmetry. Since there exist other methods, binned fits should only be used as a sanity check, but generally avoided, to circumvent the introduction of any systematics inherent to binning.

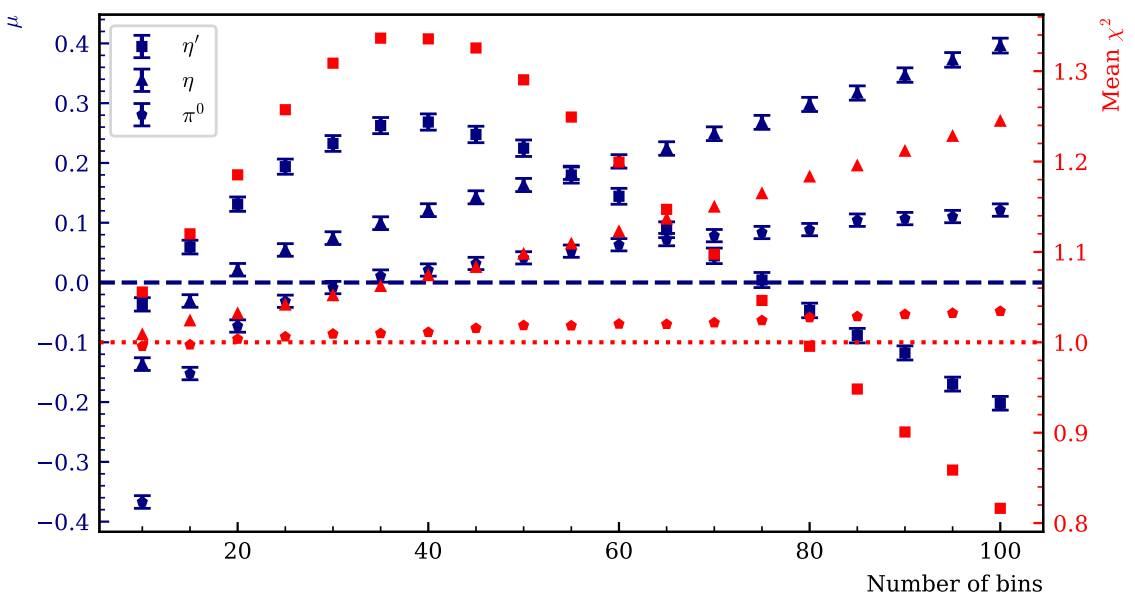


**Figure B.1:** Fit performance in dependence of the number of bins. Left axis shows the mean  $\mu$  of the distribution of the normalized residuals  $\xi$ , right axis shows the mean  $\chi^2$  of all fits. Squares simulate fits with statistics similar to the  $\gamma p \rightarrow p\eta' \rightarrow p\gamma\gamma$  final state, triangles statistics similar to the  $\gamma p \rightarrow p\eta \rightarrow p\gamma\gamma$  final state, pentagons statistics similar to the  $\gamma p \rightarrow p\pi^0 \rightarrow p\gamma\gamma$ . Dotted red line indicates the ideal value of  $\chi^2 = 1$ , while the dashed blue line indicates the ideal mean of the normalized residuals at  $\mu = 0$ .

## APPENDIX C

---

### Investigation of posteriors without truncation

---

In section 4.3 the investigation of posterior distributions from unbinned BAYESIAN fits was incomplete, since the normalized residuals as well as the likelihood pool could not be built with truncated posteriors. This is now supplemented here. After the fits have been repeated without implementing a truncation for the posteriors, all introduced measures to argue good fit quality can be examined. As a reminder, the data were generated with  $\Sigma_1 = 0.5$  and  $\Sigma_t = -0.5$ . Figure C.1 shows the combined posteriors of all fits. The left hand side shows the normalized residuals  $\Xi$  and the right hand side the unnormalized combination of all posteriors. The results completely meet the expectations, the input values for the beam asymmetries are very well reproduced, and the normalized residuals follow a standard normal distribution as GAUSSIAN fits show. Together with the results obtained from the independent likelihood pool (Figure C.2), which is able to reproduce the input values within  $1\sigma$ , this suffices to conclude correct estimation of distribution widths with no inherent bias, as had already been found in section 4.2.3.

**Remark:** It turned out that without the amount of statistics that was used in section 4.2, normal priors centered at 0 for the asymmetries  $\Sigma_t$  and  $\Sigma$  will mislead the fit results for these parameters towards 0 if no lower and upper boundaries are used. Instead the priors were then chosen to be uniform on the interval  $[-2, 2]$ . This imposes boundaries, but will not truncate the posteriors because the distributions are not expected to be this wide. All distributions shown here are generated using this model to complete the full investigation of posteriors. Previous toy Monte Carlo experiments (Figure 4.19) as well as very good agreement between point estimates and posterior distributions (Figure 4.23) together with the results shown here confirm the validity of the fit used in the main part.

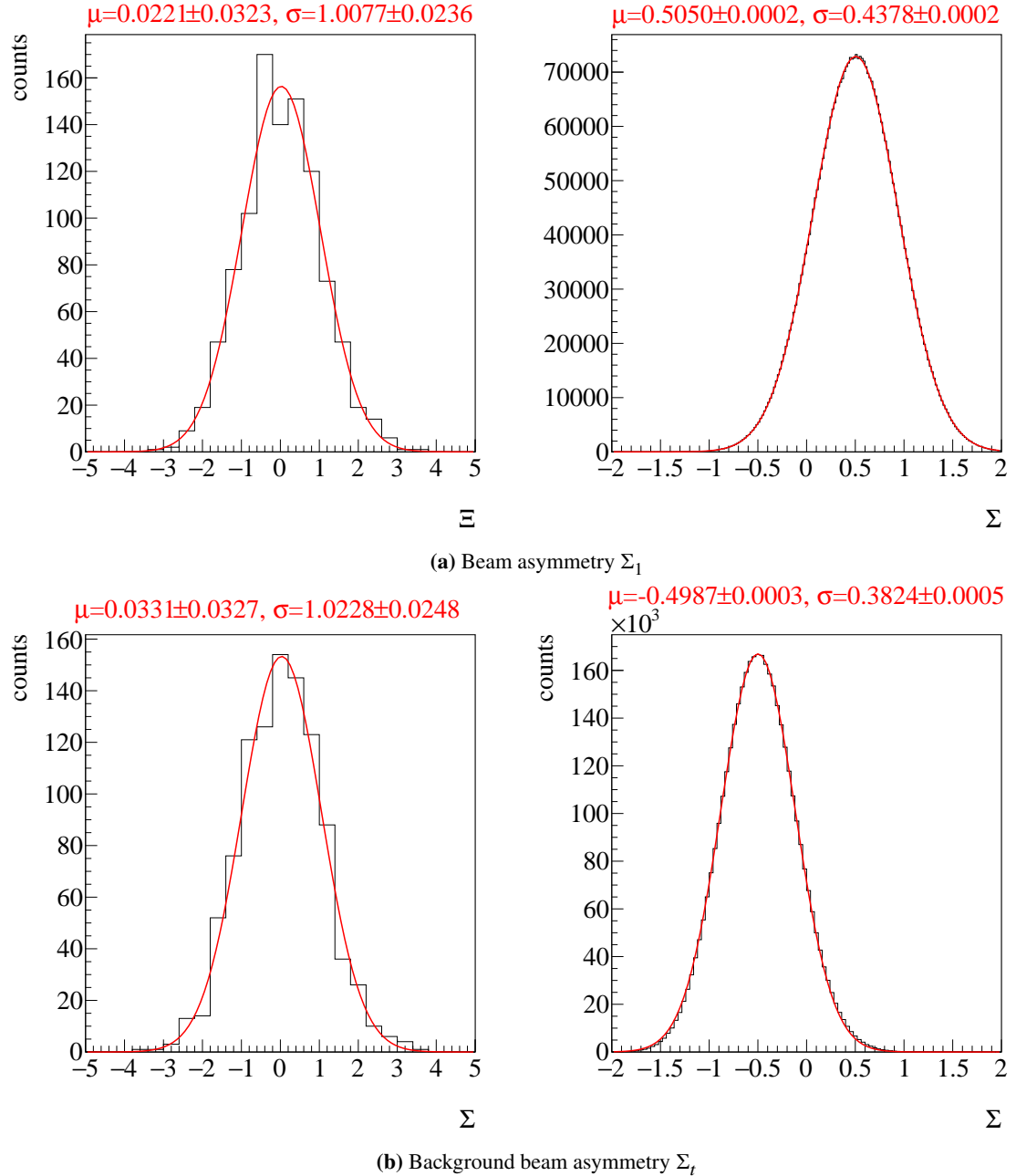


**Figure C.1:** Combined posteriors of all 1000 fits without truncation for the signal beam asymmetry  $\Sigma_1$  and the background beam asymmetry  $\Sigma_r$ . Left: normalized residuals  $\Xi$ , Right: unaltered added posterior distributions. GAUSSIAN fits have been performed with results given on top of each plot.

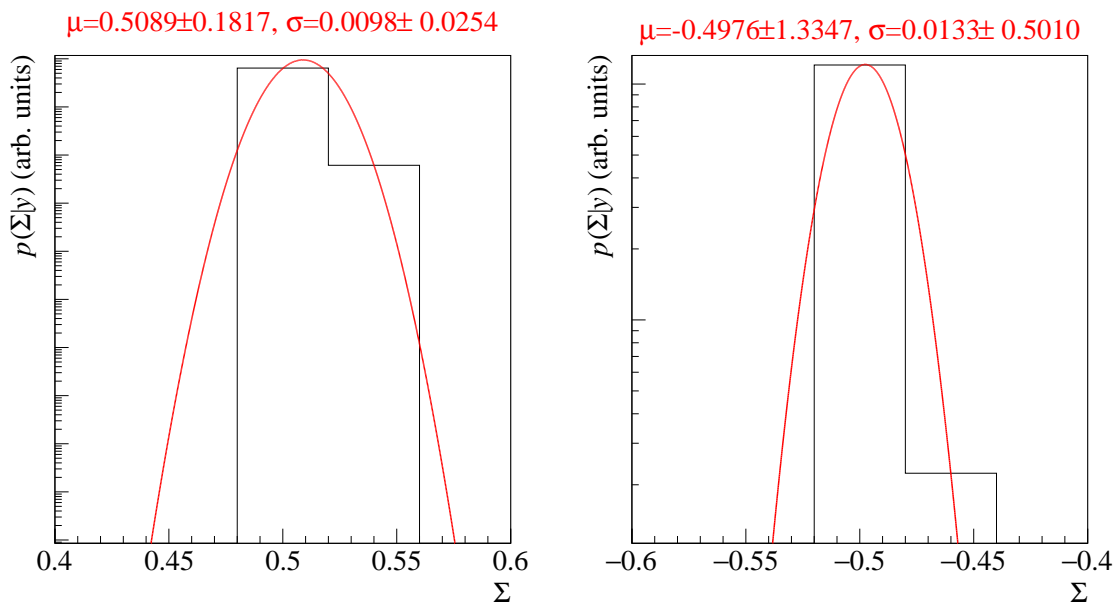


**Figure C.2:** Posterior distributions of  $\Sigma_l$  (left) and  $\Sigma_t$  (right) combined in an independent likelihood pool. GAUSSIAN fits to the distribution confirm the reproduction of the input values within  $1\sigma$ . Note that only very few datapoints were available for the fits, because the distributions overwhelmingly converge into a single bin at  $\pm 0.5$ , hence the large errors on the fit parameters.



# Bibliography

---

- [Afz12] F. N. Afzal, *Analysis of Crystal Barrel Data - Measurement of the double polarization observable  $E$  in the reaction  $\vec{\gamma}\vec{p} \rightarrow \eta' p$ ,* Master thesis: Rheinische Friedrich-Wilhelms-Universität Bonn, 2012.
- [Wor+22] R. L. Workman et al., *Review of Particle Physics*, PTEP **2022** (2022) 083C01.
- [Afz19] F. N. Afzal, *Measurement of the beam and helicity asymmetries in the reactions  $\gamma p \rightarrow p\pi^0$  and  $\gamma p \rightarrow p\eta$ ,* PhD thesis: Rheinische Friedrich-Wilhelms-Universität Bonn, 2019, URL: <https://hdl.handle.net/20.500.11811/8064> (cit. on pp. 38, 39, 43, 44, 48, 49, 53, 56, 59, 60, 68, 70).
- [Dah08] T. Dahlke, *Bestimmung einer winkelabhängigen Energiekorrekturfunktion für das TAPS-Kalorimeter des Crystal-Barrel/TAPS-Experiments und ELSA,* Diploma thesis: Rheinische Friedrich-Wilhelms-Universität Bonn, 2008.
- [GP08] M. Grüner and D.-M. Piontek, *Hit reconstruction in ChaPI*, CB-TR16 Note 003 (2008).
- [Urb17] M. Urban, *Design eines neuen Lichtpulsersystems sowie Aufbau und Inbetriebnahme der neuen APD Auslese für das Crystal-Barrel-Kalorimeter,* PhD thesis: Rheinische Friedrich-Wilhelms-Universität Bonn, 2017.
- [Ike+00] H. Ikeda et al., *A detailed test of the CsI(Tl) calorimeter for BELLE with photon beams of energy between 20-MeV and 5.4-GeV*, Nucl. Instrum. Meth. A **441** (2000) 401.
- [Cre+09] V. Crede et al., *Photoproduction of eta and eta-prime mesons off protons*, Phys. Rev. C **80** (2009) 055202, arXiv: [0909.1248 \[nucl-ex\]](https://arxiv.org/abs/0909.1248).
- [Har17] J. Hartmann, *Measurement of Double Polarization Observables in the Reactions  $\gamma p \rightarrow p\pi^0$  and  $\gamma p \rightarrow p\eta$  with the Crystal Barrel/TAPS Experiment at ELSA*, Rheinische Friedrich-Wilhelms-Universität Bonn, 2017, URL: <https://hdl.handle.net/20.500.11811/7258> (cit. on pp. 41, 43).
- [Die+20] M. Dieterle et al., *Helicity-Dependent Cross Sections for the Photoproduction of  $\pi^0$  Pairs from Nucleons*, Physical Review Letters **125** (2020), URL: <https://doi.org/10.1103%2Fphysrevlett.125.062001>.
- [Käs+18] A. Käser et al., *First measurement of helicity-dependent cross sections in  $\pi^0\eta$  photoproduction from quasi-free nucleons*, Physics Letters B **786** (2018) 305, URL: <https://doi.org/10.1016%2Fj.physletb.2018.10.006>.

## Bibliography

---

- [Bar+05] O. Bartholomy et al.,  
*Neutral-PionPhotoproduction off Protons in the Energy Range  $0.3 \text{ GeV} < E_\gamma < 3 \text{ GeV}$* ,  
Physical Review Letters **94** (2005),  
URL: <https://doi.org/10.1103%2Fphysrevlett.94.012003>.
- [Mur+20] N. Muramatsu et al., *Differential cross sections, photon beam asymmetries, and spin density matrix elements of  $\omega$  photoproduction off the proton at  $E_\gamma = 1.3 - 2.4 \text{ GeV}$* ,  
Phys. Rev. C **102** (2 2020) 025201,  
URL: <https://link.aps.org/doi/10.1103/PhysRevC.102.025201>.
- [Str+76] W. Struczinski et al., *Study of photoproduction on hydrogen in a streamer chamber with tagged photons for  $1.6 \text{ GeV} < E_\gamma < 6.3 \text{ GeV}$  Topological and reaction cross sections*,  
Nuclear Physics B **108** (1976) 45, ISSN: 0550-3213, URL:  
<https://www.sciencedirect.com/science/article/pii/0550321376901231>.
- [Dug+09] M. Dugger et al.,  
 $\pi^+$  *photoproduction on the proton for photon energies from 0.725 to 2.875 GeV*,  
Physical Review C **79** (2009),  
URL: <https://doi.org/10.1103%2Fphysrevc.79.065206>.

# List of Figures

---

1.1	Running coupling of QCD. The colored data points represent different methods to obtain a value for $\alpha_s$ . For more details it may be referred to [Wor+22]. . . . .	2
1.2	Calculated nucleon (isospin $I = 1/2$ ) resonances compared to measurements. Left in each column are the calculations [ <b>bonnmodel</b> ], the middle shows the measurements and PDG rating [Wor+22] . . . . .	3
1.3	FEYNMAN diagram for the s-channel photoproduction of pseudoscalar mesons, adapted from [Afz19] . . . . .	4
2.1	[cb] . . . . .	7
2.2	[cb] . . . . .	8
2.3	[cb] . . . . .	8
2.4	D. WALTHER in [Urb17] . . . . .	9
2.5	[cb] . . . . .	9
2.6	[cb] . . . . .	10
3.1	Distribution of event classes in $\eta' \rightarrow \gamma\gamma$ production . . . . .	13
3.2	Time information of all final state particles and the beam photon for 3PED $\eta'$ production	14
3.3	Reaction time $t_r$ for 3PED and 2.5PED $\eta'$ production. The yellow region indicate the sidebands while the purple colored interval is the selected prompt peak. . . . .	15
3.4	Coplanarity of the $p\eta'$ final state with all other cuts applied for the energy bin $1500 \text{ MeV} \leq E_\gamma < 1600 \text{ MeV}$ . The vertical dashed lines show the cut ranges obtained from a gaussian fit to the data (open circles). The solid black histograms represent fitted MC data of $\eta' \rightarrow \gamma\gamma$ . . . . .	19
3.5	Polar angle difference of the $p\eta'$ final state with all other cuts applied for the energy bin $1500 \text{ MeV} \leq E_\gamma < 1600 \text{ MeV}$ . The vertical dashed lines show the cut ranges obtained from a gaussian fit to the data (open circles). The solid black histograms represent fitted MC data of $\eta' \rightarrow \gamma\gamma$ . . . . .	20
3.6	Missing mass of the $p\eta'$ final state with all other cuts applied for the energy bin $1500 \text{ MeV} \leq E_\gamma < 1600 \text{ MeV}$ . The vertical dashed lines show the cut ranges obtained from a fit to data (open circles) employing a Novosibirsk function. The solid colored histograms represent fitted MC data from relevant photoproduction reactions: in black $\eta'$ , in green $\pi^0$ , in red $\eta$ , in blue $\omega$ , in yellow $2\pi^0$ , magenta $\pi^0\eta$ . The turquoise histogram is the sum of all MC histograms. . . . .	21

3.7	Invariant mass of the $p\eta'$ final state with all other cuts applied for all energy and angular bins. The open circles represent the measured data, the solid colored histograms fitted MC data from relevant photoproduction reactions: in black $\eta'$ , in green $\pi^0$ , in red $\eta$ , in blue $\omega$ , in yellow $2\pi^0$ and in magenta $\pi^0\eta$ . The turquoise histogram is the sum of all MC histograms. . . . .	22
3.8	Invariant mass of the $p\eta'$ final state with all other cuts applied for the energy bin $1500 \text{ MeV} \leq E_\gamma < 1600 \text{ MeV}$ . The vertical dashed lines show the cut ranges obtained from a gaussian fit to the $\eta'$ MC data (solid black histogram). The open circles represent the measured data, the solid colored histograms fitted MC data from relevant photoproduction reactions: in black $\eta'$ , in green $\pi^0$ , in red $\eta$ , in blue $\omega$ , in yellow $2\pi^0$ and in magenta $\pi^0\eta$ . The turquoise histogram is the sum of all MC histograms. . . . .	22
3.9	Acceptance for the reaction $\gamma p \rightarrow p\eta'$ after all cuts that have been discussed so far for 2.5PED and 3PED events . . . . .	23
3.10	Fraction of background events in the analyzed beam energy and angular bins. . . . .	24
3.11	Acceptance for possible background contributions . . . . .	25
3.12	Generated energies of $\gamma_3$ and $\gamma_4$ in $2\pi^0$ and $\pi^0\eta$ photoproduction MC data. The threshold of 20 MeV is marked by a vertical red line. $E_{\gamma_4}$ is shown on the top, $E_{\gamma_3}$ is shown on the bottom of each figure. . . . .	27
3.13	$E_\gamma^{\text{gen}}$ vs. $E_\gamma^{\text{rec}}$ of $\gamma_1$ and $\gamma_2$ for $2\pi^0$ (top) and $\pi^0\eta$ (bottom) production. The slope $E_\gamma^{\text{gen}} = E_\gamma^{\text{rec}}$ is marked by a solid line. . . . .	29
3.14	Polar angle difference $\Delta\theta$ between $\gamma_2$ and $\gamma_3$ of the $\pi^0\eta$ final state. . . . .	30
3.15	Illustration of the misidentification process during reconstruction. Enumeration of photons is now arbitrary. . . . .	30
3.16	Generated CMS angle $\cos\theta_{\text{gen.}}$ vs. reconstructed CMS angle $\cos\theta_{\text{rec.}}$ for both background reactions. The slope $\cos\theta_{\text{gen.}} = \cos\theta_{\text{rec.}}$ is indicated by the solid line. . . . .	31
3.17	Detector hits of the recoil proton, as obtained from MC data for the production of $\eta'$ , $2\pi^0$ and $\pi^0\eta$ . CB: Crystal Barrel, FW: forward dector, MT: MiniTAPS . . . . .	33
3.18	Difference in measured and calculated beam energy. Data points are shown as open circles, MC data as solid histograms: in black $\eta'$ , in green $\pi^0$ , in red $\eta$ , in blue $\omega$ , in yellow $2\pi^0$ and in magenta $\pi^0\eta$ . The turquoise histogram is the sum of all MC histograms. . . . .	34
3.19	Invariant mass spectrum passing different stages in the event selection process. In the end clear peaks for all possibly produced mesons are visible. The vertical lines indicate the mean cut ranges over all energy and angle bins. . . . .	35
3.20	Invariant mass spectrum passing different stages in the event selection process. In the end clear peaks for all possibly produced mesons are visible. Taken from [Afz19]. . . . .	36
4.1	Left: Definition of angles $\alpha, \phi, \varphi$ . Right: Photon momentum $\vec{k}$ and polarization $\vec{\epsilon}$ define the beam polarization plane while the reaction plane is defined by the recoil proton $p$ and produced meson $M$ . . . . .	37

4.2 Posterior predictive checks $p(A_{\text{rep}} A)$ from a BAYESIAN fit to the event yield asymmetries for six toy Monte Carlo bins are shown as distributions. The data points in the upper plot are the asymmetry $A(\phi)$ , which was additionally fitted using a $\chi^2$ fit (solid line). The goodness of fit is shown using $p$ -values, which give the fraction $T(A_{\text{rep}} > A)$ of replicated samples greater than the original measured value, with propagated statistical error bars on the bottom of each plot. The expected mean value of $T(A_{\text{rep}} > A) = 0.5$ is indicated by the dashed line.	46
4.3 $p$ values of all toy Monte Carlo bins. They are centered around their mean at 0.5, which is indicated by the dashed line, and show no bias towards higher or lower values, thus confirming an adequate fit.	47
4.4 Left: Combined posterior distributions of all 10000 fits normalized by their respective standard deviation. Right: Unaltered combined posterior distributions of all 10000 fits. A GAUSSIAN fit was performed to determine mean $\mu$ and standard deviation $\sigma$ of the distributions with results given on top.	47
4.5 Left: relative error $\frac{\sigma_{\text{MCSE}}}{\text{median}[p(\Sigma y)]}$ Right: $\widehat{R}$ associated with the fit parameter $\Sigma$ . Both are shown for all 10000 fits. The critical values that should not be exceeded are marked by dashed lines.	48
4.6 Combined posteriors for the beam asymmetries $\Sigma$ and $\Sigma^{\text{bkg}}$ from all 1000 event based fits. Left: Residuals $\Xi$ Right: Unnormalized posterior distributions. A GAUSSIAN fit is performed on the distributions with results for mean $\mu$ and standard deviation $\sigma$ on top.	50
4.7 Combined posterior probabilities using the <i>pooled likelihood</i> approach. Left: Signal beam asymmetry, Right: background beam asymmetry. Mean and standard deviation as obtained from a Gaussian fit are shown on top	51
4.8 Left: relative error $\frac{\sigma_{\text{MCSE}}}{\text{median}[p(\Sigma y)]}$ Right: $\widehat{R}$ associated with the fit parameter $\Sigma$ . Both are shown for all 1000 fits. The critical values that should not be exceeded are marked by dashed lines.	51
4.9 Posterior predictive check using the draws of the detector coefficients $a$ and $b$ . Points with error bars are the polarization weighted sum of event yields. The dashed line is the mean of the predictive values while the solid opaque lines are representative of one simulation draw $a^{(s)}, b^{(s)}$ .	52
4.10 Posterior predictive checks $p(A_{\text{rep}} A)$ from a BAYESIAN fit to the event yield asymmetries for all angular bins of the energy bin $1250 \text{ MeV} \leq E_\gamma < 1310 \text{ MeV}$ . The data points in the upper plot are the asymmetry $A(\phi)$ , which was additionally fitted using a $\chi^2$ fit (solid line). The goodness of fit is shown using $p$ -values, which give the fraction $T(A_{\text{rep}} > A)$ of replicated samples greater than the original measured value, with propagated statistical error bars on the bottom of each plot. The expected mean value of $T(A_{\text{rep}} > A) = 0.5$ is indicated by the dashed line.	54
4.11 $p$ values generated using all fits. They are centered around their mean at 0.5, which is indicated by the dashed line, and show no bias towards higher or lower values, thus confirming an adequate fit.	55
4.12 Left: relative error $\frac{\sigma_{\text{MCSE}}}{\text{median}[p(\Sigma y)]}$ Right: $\widehat{R}$ associated with the fit parameter $\Sigma$ . Both are shown for all $11 \cdot 12$ binned fits to the asymmetry $A(\phi)$ . The critical values that should not be exceeded are marked by dashed lines.	55

4.13 Left: relative error $\frac{\sigma_{\text{MCSE}}}{\text{median}[p(\Sigma y)]}$	Right: $\widehat{R}$ associated with the fit parameter $\Sigma$ . Both are shown for all $11 \cdot 12$ unbinned fits. The critical values that should not be exceeded are marked by dashed lines.	56
4.14 Posterior predictive check using the draws of the detector coefficients $a$ and $b$ for the kinematic bin $1250 \text{ MeV} \leq E_\gamma < 1310 \text{ MeV}, 0 \leq \cos \theta < 0.17$ . Points with error bars are the polarization weighted sum of event yields. The dashed line is the mean of the predictive values while the solid opaque lines are representative of one simulation draw $a^{(s)}, b^{(s)}$ .	57	
4.15 Final results for the beam asymmetry $\Sigma$ in $\eta$ photoproduction off the proton for all kinematic bins obtained with BAYESIAN methods. They are compared with the results of a least squares fit and an unbinned fit as given in reference [Afz19]. All results agree within statistical error bars or within the widths of marginal posterior distributions.	59	
4.16 Normalized residuals (left) and unaltered distribution (right) of all 10000 fits for the beam asymmetry $\Sigma = (1 - \delta) \cdot \Sigma_1 + \delta \cdot \Sigma_2$ . GAUSSIAN fits are performed with results given on top of each plot.	61	
4.17 Normalized residuals (left) and unaltered distribution (right) of all 10000 fits for the background beam asymmetry $\Sigma_t^{\text{bkg}}$ . GAUSSIAN fits are performed with results given on top of each plot.	62	
4.18 Fitted efficiency function (red line) applied to the polarization weighted sum of event yields (data points) for one toy Monte Carlo bin. 12 bins in $\phi$ are built for demonstration.	62	
4.19 Combined (added) posteriors of all 1000 fits. Left: Signal beam asymmetry $\Sigma_1$ Right: Background beam asymmetry $\Sigma_t^{\text{bkg}}$ . A GAUSSIAN fit is performed with results given on top.	63	
4.20 Combined (added) posteriors of all fits for the fit parameter $\Sigma_2^{\text{true}}$ . A GAUSSIAN fit is performed which reproduces exactly the values that were used for the simulations.	64	
4.21 MCMC diagnostics for the event based BAYESIAN fit. Left: MCSE, Right: $\widehat{R}$ -value. The critical values not to be exceeded are marked by the dashed lines.	65	
4.22 Posterior predictive checks of one toy Monte Carlo bin using the draws from the marginal posteriors of the detector coefficients $a, b$ (opaque blue lines). The mean values are marked by the dashed line and follow the distribution of the data points which are the polarization weighted sum of event yields, using 12 $\phi$ bins.	65	
4.23 Final results for the beam asymmetry $\Sigma$ in $\eta'$ photoproduction. Two sets of results are shown: The dark blue distributions and orange data points with errorbars are obtained with an unbinned fit that does not consider any background contributions. The light blue distributions and data points are obtained with the modified BAYESIAN fit and by correcting the point estimates according to Equation (4.42), respectively. All errors are statistical errors only.	67	
4.24 Results for the additionally fitted $\Sigma_2^{\text{true}}$ (distributions) compared with the underlying data points [ <b>mahlbergphd</b> ] with statistical errors. The error bars on average cover $1\sigma$ of the distributions, indicating a successful fit. All errors are statistical errors only.	68	
4.25 MCMC diagnostics for the event based BAYESIAN fit. Left: MCSE, Right: $\widehat{R}$ -value. The critical values not to be exceeded are marked by the dashed lines.	69	

4.26 Posterior predictive checks of the kinematic bin $1700 \text{ MeV} \leq E_\gamma < 1800 \text{ MeV}$ , $0.67 \leq \cos \theta < 1$ using the draws from the marginal posteriors of the detector coefficients $a, b$ (opaque blue lines). The mean values are marked by the dashed line and follow the distribution of the data points which are the polarization weighted sum of event yields, using 12 $\phi$ bins. . . . .	69
4.27 Final results for the beam asymmetry $\Sigma_{\eta'}$ for all energy and angular bins. Only the corrected results from the unbinned maximum likelihood fit and distributions from the modified BAYESIAN fit are shown. The bottom of each plot indicates the systematic error as gray bars. It was determined as previously discussed. . . . .	71
A.1 Coplanarity $\Delta\phi$ for all energy and angular bins. Data points are displayed as open circles, scaled Monte Carlo data belonging to $\eta'$ photoproduction is displayed as solid histogram. The determined cut ranges are indicated by the dashed red lines. . . . .	67
A.1 Coplanarity $\Delta\phi$ for all energy and angular bins. Data points are displayed as open circles, scaled Monte Carlo data belonging to $\eta'$ photoproduction is displayed as solid histogram. The determined cut ranges are indicated by the dashed red lines. . . . .	68
A.2 Polar angle difference $\Delta\theta$ for all energy and angular bins. Data points are displayed as open circles, scaled Monte Carlo data belonging to $\eta'$ photoproduction is displayed as solid histogram. The determined cut ranges are indicated by the dashed red lines. . . . .	69
A.2 Polar angle difference $\Delta\theta$ for all energy and angular bins. Data points are displayed as open circles, scaled Monte Carlo data belonging to $\eta'$ photoproduction is displayed as solid histogram. The determined cut ranges are indicated by the dashed red lines. . . . .	70
A.3 Missing mass $m_x$ for all energy and angular bins. Data points are displayed as open circles, scaled Monte Carlo data belonging to $\eta'$ (black), $2\pi^0$ (yellow) and $\pi^0\eta$ (magenta) photoproduction is displayed as solid histogram while their sum is displayed as turquoise histogram. The determined cut ranges are indicated by the dashed red lines. . . . .	71
A.3 Missing mass $m_X$ for all energy and angular bins. Data points are displayed as open circles, scaled Monte Carlo data belonging to $\eta'$ (black), $2\pi^0$ (yellow) and $\pi^0\eta$ (magenta) photoproduction is displayed as solid histogram while their sum is displayed as turquoise histogram. The determined cut ranges are indicated by the dashed red lines. . . . .	72
A.4 Invariant mass $m_{\text{meson}}$ for all energy and angular bins. Data points are displayed as open circles, scaled Monte Carlo data belonging to $\eta'$ (black), $2\pi^0$ (yellow), $\pi^0\eta$ (magenta), $\pi^0$ (green) and $\omega$ (blue) photoproduction is displayed as solid histogram while their sum is displayed as turquoise histogram. The determined cut ranges are indicated by the dashed red lines. . . . .	73
A.4 Invariant mass $m_{\text{meson}}$ for all energy and angular bins. Data points are displayed as open circles, scaled Monte Carlo data belonging to $\eta'$ (black), $2\pi^0$ (yellow), $\pi^0\eta$ (magenta), $\pi^0$ (green) and $\omega$ (blue) photoproduction is displayed as solid histogram while their sum is displayed as turquoise histogram. The determined cut ranges are indicated by the dashed red lines. . . . .	74

B.1	Fit performance in dependence of the number of bins. Left axis shows the mean $\mu$ of the distribution of the normalized residuals $\xi$ , right axis shows the mean $\chi^2$ of all fits. Squares simulate fits with statistics similar to the $\gamma p \rightarrow p\eta' \rightarrow p\gamma\gamma$ final state, triangles statistics similar to the $\gamma p \rightarrow p\eta \rightarrow p\gamma\gamma$ and final state, pentagons statistics similar to the $\gamma p \rightarrow p\pi^0 \rightarrow p\gamma\gamma$ . Dotted red line indicates the ideal value of $\chi^2 = 1$ , while the dashed blue line indicates the ideal mean of the normalized residuals at $\mu = 0$ .	76
C.1	Combined posteriors of all 1000 fits without truncation for the signal beam asymmetry $\Sigma_1$ and the background beam asymmetry $\Sigma_t$ . Left: normalized residuals $\Xi$ , Right: unaltered added posterior distributions. GAUSSIAN fits have been performed with results given on top of each plot.	78
C.2	Posterior distributions of $\Sigma_1$ (left) and $\Sigma_t$ (right) combined in an independent likelihood pool. GAUSSIAN fits to the distribution confirm the reproduction of the input values within $1\sigma$ . Note that only very few datapoints were available for the fits, because the distributions overwhelmingly converge into a single bin at $\pm 0.5$ , hence the large errors on the fit parameters.	79

# List of Tables

---

1.1	Summary of the particles of the SM . . . . .	1
1.2	Allowed quantum numbers for the intermediate resonance state $N^*/\Delta^*$ . . . . .	4
3.1	The five most probable decay modes of the $\eta$ and $\eta'$ meson. The most probable further decay with according branching ratio is shown in brackets.[Wor+22] . . . . .	11
3.2	Examined MC reactions that were used in sum for the fit . . . . .	17
3.3	Fit functions and cut ranges for each kinematic variable . . . . .	18
3.4	Total cross sections $\sigma$ in the energy range 1500 to 1800 MeV, branching ratios (BR) to $n\gamma$ final states, maximum acceptance $\tilde{A}$ for signal and possible background contributions as well as the expected signal to background ratio $R$ . References [Die+20] and [Käs+18] give the cross sections only up to roughly 1500 MeV, the given values are thus upper bounds. For the same reason, from reference [3pi0cs] only a lower bound can be estimated. For all other reactions a rough mean over the energy bins of interest is built. If the references provide only differential cross sections a crude integration in each angular bin is performed. In case only very few ( $O(10^1)$ ) decays pass event selection, the acceptance is built in one global bin only for the respective reactions. This is indicated by the horizontal line. . . . .	26
3.5	Relative loss in signal and background events if a cut on $\Delta E$ is applied. . . . .	32
4.1	Summary of the complete setting of all toy Monte Carlo experiments for the event based fit. Values and table layout adapted from [Afz19]. . . . .	49
4.2	Summary of the complete setting of all toy Monte Carlo experiments for the event based fit. Table layout adapted from [Afz19]. . . . .	60